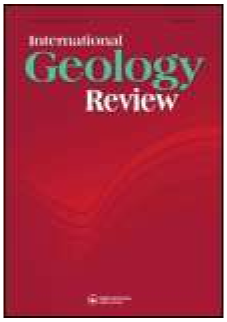

Alpine convergence record in the Carboniferous Badstub Formation, Upper Austroalpine basement nappes, Austria

Journal:	*International Geology Review*
Manuscript ID	TIGR-2022-0292.R4
Manuscript Type:	Research Article
Date Submitted by the Author:	n/a
Complete List of Authors:	Zanoni, Davide; Università degli Studi di Milano, Scienze della Terra Ardito Desio Filippi, Marco; Università degli Studi di Milano, Scienze della Terra Ardito Desio Roda, Manuel; Università degli Studi di Milano, Scienze della Terra Ardito Desio Regorda, Alessandro; Università degli Studi di Milano, Scienze della Terra Ardito Desio Spalla, Maria Iole; Università degli Studi di Milano, Scienze della Terra Ardito Desio
Keywords:	Alpine subduction, Palaeozoic sequences, geodynamic modelling, Alpine pumpellyite prehnite riebeckite, Drauzug-Gurktal Nappe System

Alpine convergence record in the Carboniferous Badstub Formation, Upper Austroalpine basement nappes, Austria

Davide Zanoni[a]*, Marco Filippi[a], Manuel Roda[a], Alessandro Regorda[a], and Maria Iole Spalla[a]

[a]*Dipartimento di Scienze della Terra "A. Desio", Università degli Studi di Milano, Milano, Italy*

*Corresponding author: Dipartimento di Scienze della Terra "A. Desio", Università degli Studi di Milano, via Mangiagalli, 34, 20133, Milano Italy; davide.zanoni@unimi.it

Orcid ID:

Davide Zanoni: 0000-0003-1404-4824

Marco Filippi: 0000-0003-2183-7259

Manuel Roda: 0000-0002-5446-6434

Alessandro Regorda: 0000-0002-7677-4542

Maria Iole Spalla: 0000-0001-8346-5070

Alpine convergence record in the Carboniferous Badstub Formation, Upper Austroalpine basement nappes, Austria

Within the Carboniferous of Nötsch, the Badstub Formation is a clastic sequence of the Upper Austroalpine basement nappes exposed few kilometres north of the Periadriatic Fault System (Carinthia, Austria). Although these rocks preserve pristine sedimentary features, multi-scale structural analysis disclosed a syn-metamorphic foliation in fine-grained rocks, sets of mineralised faults, veins, and corona textures. Vein fillings and coronas contain equilibrium mineral assemblages with prehnite, pumpellyite, chlorite, phengitic mica, winchite, and riebeckite. Thermodynamic modelling and geothermometry constrain metamorphic conditions at 260 - 310 °C and 0.25 - 0.50 GPa that are consistent with a temperature / depth ratio of about 20 °C km^{-1}. In a 2D thermomechanical model this thermal state is reached either in the upper or lower continental plate during convergence. Thus, during the Alpine convergence, the Badstub rocks were buried from the shallow crust at depths between 13 and 18 km either by ablative oceanic subduction or by continental subduction of the passive margin, and eventually stacked into the orogenic wedge at the Adria margin. During the downward and upward path, the Badstub rocks were translated as a coherent poorly strained block. This first quantitative constraint on metamorphism for these Carboniferous rocks is consistent with the Upper Austroalpine basement nappes being a tectonic system that recorded the Alpine convergence under eclogite to prehnite-pumpellyite facies conditions.

Keywords: Alpine pumpellyite prehnite riebeckite; Alpine subduction; Palaeozoic sequences; geodynamic modelling; Drauzug-Gurktal Nappe System.

1. Introduction

The Austroalpine and Penninic domains of the Alps constitute the axial part of the Alpine chain that is confined by the Penninic front to the north and the Periadriatic Fault System to the south. During the Alpine convergence rocks belonging to these domains recorded pervasive deformation and metamorphism at different structural levels and under various geothermal gradients (e.g., Frey *et al.* 1999; Schuster *et al.* 2004;

Lardeaux 2014). However, in the Eastern Alps the upper part of the Austroalpine nappe stack includes rock sequences that were only weakly to partially deformed and metamorphosed. Here, sedimentary rocks well preserve stratigraphic features. Among those rock units, the Carboniferous of Nötsch is part of the Palaeozoic sequences of the Drauzug-Gurktal Nappe System exposed between the Drau and Gail valleys (Figure 1a) and is even famous for the outstanding fossil records. As a result, many palaeontological and stratigraphic studies have been undertaken to shed light on the environmental significance of this formation in the frame of the Palaeozoic palaeogeography (Sieber 1972; Schraut 1999; Vachard *et al*. 2018). Moreover, studies on the Carboniferous of Nötsch were focused on clasts for discussing their origin (Exner 1983; Krainer and Mogessie 1991).

The Carboniferous of Nötsch records low-grade metamorphism for which only temperature is constrained (Rantitsch *et al.* 1995). This contribution includes new field, microstructural, and mineral chemical data from the Badstub Formation, a stratigraphic unit of the Carboniferous of Nötsch, to constrain the metamorphic temperature and pressure and the tectono-metamorphic record. Since the excellent rock exposure, we concentrate our analysis in the Jakomini quarry, which is in the Nötschbach valley, a few kilometres north of the Nötsch im Gailtal village in southern Carinthia, Austria (Figure 1b). Regardless the pristine sedimentary features clearly detectable at first glance on rock outcrops, the multi-scale structural analysis discloses tectonic and metamorphic overprints on sedimentary structures. We individuate microstructural domains with mineral assemblages suitable for quantifying metamorphic conditions by thermometrical estimates and thermodynamic modelling. The estimated metamorphic conditions are compared with the predictions of a 2D thermomechanical numerical model to test the most reliable geodynamic scenarios under which the detected tectono-metamorphic record of Badstub Formation developed.

2. Geological setting

The eastern Austroalpine domain is divided into the Lower and Upper Austroalpine basement nappes (Figure 1a) that both consist of basement and cover nappes generally interpreted as deriving from the outer and inner portions of the Adriatic passive margin, respectively (Schmid *et al.* 2004). The Upper Austroalpine basement nappes are divided into four stacked nappe systems of which the uppermost is the Drauzug-Gurktal Nappe System (Schmid *et al.* 2004). Most tectonic units of the Upper Austroalpine basement nappes record successive tectono-metamorphic imprints: a Variscan metamorphism characterised by a high-pressure peak; a Permian metamorphism characterised by low-pressure medium temperature conditions; a Cretaceous (Eo-Alpine) metamorphism characterised by high pressure peak and P/T ratios and related to the Alpine subduction (Hoinkes *et al.* 1999; Neubauer *et al.* 1999a, 1999b; Habler and Thöni 2001; Faryad and Hoinkes 2003; Kurz and Fritz 2003; Schuster and Stüwe 2008; Krenn *et al.* 2011; Roda *et al.* 2012; Rode *et al.* 2012; Sandmann *et al.* 2016; Hauke *et al.* 2019; Li *et al.* 2021).

The Upper Austroalpine basement nappes include Palaeozoic and Mesozoic rock assemblages. Within the Drauzug-Gurktal Nappe System, weakly metamorphosed Palaeozoic sequences outcrop in the Gurktal nappes, Carboniferous of Nötsch, Palaeozoic of Graz, Remschnigg and Sausal areas, and southern Burgenland (Piller, 2014). The Carboniferous of Nötsch extends about 9 and 3 km in east-west and north-south direction, respectively, and is comprised between the Permian-Triassic carbonate and sandstone sequences of the Drau Range to the north, and the Gailtal crystalline basement to the south (Hauser *et al.* 1982; Krainer 1993; Schönlaub 1985). The Carboniferous of Nötsch outcrops adjacent to the Gailtal Line, which is the eastern segment of the Periadriatic Fault System, is separated from the crystalline basement by tectonic boundaries, and is capped by about 5 km-thick sequence of Permian to Mesozoic rocks at its eastern edge (Figure 1b) (Tollmann 1977). From bottom to top, the Carboniferous of Nötsch, consists of a continuous litostratigraphy (Supp. Table 1): Erlachgraben Formation, Badstub Formation, and Nötsch Formation (Schönlaub 1985; Krainer 1992; Krainer and Vachard 2002; Vachard *et al.* 2018). The Carboniferous of Nötsch displays upper Visean and lower Kasimovian strata (Ebner *et al.* 2008; Piller 2014) and the Badstub Formation is Serpukhovian in age (Vachard *et al.* 2018).

The Badstub Formation (Figure 1b) consists of amphibolite breccia, conglomerate, sandstone, and siltstone sequences that are interpreted as submarine re-sedimented deposits by gravity flows (Krainer and Mogessie 1991; Krainer 1992). In the Badstub Formation exotic clasts derived from a carbonate shelf developed on the northern margin of the western Palaeotethys (Vachard *et al.* 2018) in the foreland of the Variscan belt (Krainer and Vachard 2002). The Badstub Formation contains abundant clasts of amphibolites, metagranitoids, paragneisses, schists, quartzites, and marbles (Krainer and Mogessie 1991; Schönlaub and Heinisch 1994). The dominant clasts are rich in Mg- and Fe-hornblende and derive from metamorphosed tholeiitic basalts (Krainer and Mogessie 1991; Vignaroli *et al.* 2013). The abundance of pristine coarse-sized amphibolite clasts indicates rapid sedimentation triggered by active fault zones (Krainer and Mogessie 1991).

The Carboniferous of Nötsch outcrops south of the SAM (southern border of the Alpine metamorphism, Figure 1a; Hoinkes *et al.* 1999; Schuster *et al.* 2004) line. North of the SAM line, the Upper Austroalpine basement nappes record Cretaceous metamorphism. The grade of the dominant metamorphic imprint increases from the Silvretta Seckau-Nappe System, which records anchizonal to epidote-amphibolite facies conditions, up to the centre of the Koralpe-Wölz Nappe System, which records greenschist to eclogite facies conditions. From the centre of the Koralpe-Wölz Nappe System, the grade of the dominant metamorphism decreases structurally upward and indeed the Ötztal-Bundschuh and Gurktal-Drauzug Nappe Systems record anchizonal to amphibolite facies conditions (Haüy 1822; Faryad and Hoinkes 2003; Schuster *et al.* 2004; Froitzheim *et al.* 2008; Krenn *et al.* 2011; Janák *et al.* 2004, 2015; Schulz 2017; Hauke *et al.* 2019; Rantitsch *et al.* 2020; Li *et al.* 2021; Schorn *et al.* 2021; Schuster and Stüwe 2022). South of the SAM line, minerals such as prehnite and analcime are described in the Badstub Formation (Niedermayr *et al.* 2010) and very low-grade Alpine metamorphism in the Carboniferous of Nötsch is constrained based on illite crystallinity and vitrinite reflectance at 260 °C and 6 km depth (Rantitsch 1995). In the Permian to Cretaceous sedimentary sequences of the western Drau Range, Alpine anchizonal metamorphism is constrained at temperatures lower than 270 °C and pressures around 0.2 GPa based on illite crystallinity (Niedermayr *et al.* 1984; Rantitsch 2001), whereas Alpine greenschist facies metamorphism is inferred in basement rocks of Goldeck mountains (Deutsch 1988). In the regions surrounding the Carboniferous of Nötsch, diagenetic to very low-grade Alpine metamorphism is also documented in the Gurktal Nappe (Rantitsch and Russegger 2000; Rantitsch *et al.* 2020) and Carnic Alps just to the south of the Periadriatic Fault System (Läufer *et al.* 1997; Rantitsch 1997; Rantitsch *et al.* 2000). The low grade metamorphic peak temperatures are supposed to be Cretaceous in age and related to nappe staking during the Alpine convergence (Rantitsch *et al.* 2020), whereas they are constrained at the Oligocene in the Carnic Alps and related to the strike-slip deformation along the Periadriatic Fault System (Läufer *et al.* 1997).

3. Lithostratigraphy

We focused our field survey in the Jakomini quarry (Figure 2) where the best outcrop of Badstub Formation is exposed (see also Schönlaub in Piller 2014). The mined rocks are entirely part of the middle sequence of the Badstub Formation of the Carboniferous of Nötsch. They consist of breccia, conglomerate, sandstone, and minor siltstone and pelite and are heterogeneously deformed, but with well-preserved primary textures. Therefore, protholit names are used except for finely foliated carbonatic rocks referred as fossiliferous schist. Based on the litostratigraphy and meso- and micro-textural features (see also Vignaroli *et al.* 2013) four zones have been distinguished in the quarry (Figure 2), which from north to south we name: CSS (conglomerate, sandstone, and siltstone), DCB (dominant conglomerate and breccia), FS (fossiliferous schist), and CB (conglomerate and breccia). Although the boundaries between DCB and FS, and FS and CB are sharp, the limit between CSS and DCB is gradational. From CSS to CB, the stratigraphic top of the sedimentary sequence is reached.

CSS - This zone is exposed in the northernmost part of the quarry and (Figure 2) is characterised by reddish breccia, conglomerate, conglomeratic breccia, sandstone, and siltstone. Matrix- and locally clast-supported conglomerate and breccia dominate in the northern and southern part of this sector (Figure 3a), whereas dozen metre-thick siltstone and sandstone sequences dominate the central part. Millimetre- to decimetre-sized angular to sub-rounded clasts consist of metabasite (amphibolite), and minor marble and metaintrusives (metadiorite and metatonalite). Metabasic clasts are more abundant in the upper portion of CSS and in the central southern part, decimetre-thick conglomerate beds are rich of marble clasts (Figure 3b). Leucocratic metagranitoid and marble clasts are also locally abundant in the lower part. Two decimetre-thick beds of fossiliferous schist with brachiopods outcrop nearby the junction of "*etage*" 805 and

820 (Figure 2). Close to the transition with sector DCB, in "*etage*" 790, decimetre-sized lenses contain metabasic clasts cemented by calcite.

DCB - Here rocks have intermediate composition compared to CSS and CB, and they mostly consist of conglomerate and breccia with dominant mafic components and are either clastic or sandy matrix-supported. Locally rocks contain a red silty matrix like in CSS. Angular to sub-rounded clasts are mostly metabasic with minor centimetre- to decimetre-sized marble clasts (Figure 3c). The conglomerate forms metre-thick beds interbedded with decimetre-thick mafic sandstone and red siltstone beds (Figure 3d) and forms up to metre-thick sequences. Locally the conglomerate with centimetre-sized metabasite clasts shows calcite cement distributed along centimetre-thick and 1- to 2-metre-long layers and lenses (Figure 3e).

FS - The rocks ("Zwischenschiefer") consist of black fossiliferous schists with up to decimetre-sized carbonatic bioclasts, such as brachiopods, foraminifera, and crinoids. These rocks are finely laminated and form a 10- to 15-metre-thick sequence (Figure 3f). Brachiopods are articulated and mostly iso-oriented with the convex side toward the stratigraphic bottom. Often these rocks contain a pervasive tectonic cleavage.

CB - Rocks consist of mafic breccia and minor conglomerate that form metre-thick beds with fining upward sequences. The boundaries between these sequences are marked by centimetre-thick layer of siltstone and pelite (Figure 3g). The texture of conglomerate and breccia is mainly clast-supported, and mainly rounded clasts consist of metabasic, and rare marble and leucocratic metagranitoid rocks (Figure 3h). Clast dimension varies between few millimetres to few decimetres and larger clasts consist of marble, which are more abundant close to the boundary with FS. Locally rocks display carbonatic cement. In CB the rocks show the highest clast concentration (up to 90%). A carbonatic siltstone with bioclasts outcrops in the very southernmost edge of the quarry at lower elevation and is rich in crinoids.

4. Mesostructures

The dominant structure in the quarry is the bedding, S0, (Figure 4a) that shows dip direction toward south or southwest (Figure 2, inset a). A cleavage (S1) is developed mostly in the black fossiliferous schist in FS and locally in the sandstone and siltstone in CSS (Figure 4b and 4c). In the fossiliferous schist, S1 foliation is asymptotic to calcite veins suggesting a shearing accommodated along the vein walls (Figure 4d) that intersects S1. S1 is a slaty cleavage in fossiliferous schist and a slightly refracted spaced foliation in sandstone and siltstone. S1 is steeper than the bedding and dips generally southwestward (Figure 2, inset a). Due to the refraction in finer-grained rocks locally S1 parallels S0 especially at strata boundaries. The faults show different orientation and kinematics, and up to metre-thick cataclastic bands (Figure 4a). Calcite fibres developed also on fault surfaces sub-parallel to the quarry front (Figure 4e) and fault surfaces mineralised with hematite fibres are detected in CSS and DCB. Millimetre- to centimetre-thick veins are filled mainly by calcite but also by chlorite and epidote (Figure 4f). Calcite veins crosscut chlorite and epidote veins.

The main fault system is steeply dipping and strikes NNE-SSW, sub-parallel to the quarry front (Figure 4a, Figure 2, inset b) and sub-parallel to the main regional strike-slip fault systems (Figure 1b). Kinematic indicators suggest a dextral or sinistral transtensive displacement (Figure 2, inset b). A conjugate fault system shows north-northwest and northeast striking surfaces with dip between 30° and 50° (Figure 2, inset b). Both fault surfaces accommodate a reverse and normal kinematic and developed decimetre-thick cataclastic bands.

5. Microstructures

Microstructural analysis focused on deformation fabrics and metamorphic textures that overprinted the primary sedimentary features (sample locations are in Figure 2). Due to the heterogeneous deformation, metamorphic minerals constitute structures such as tectonitic foliations, mineral coronas, and veins.

In the studied sequence, the clasts mostly consist of foliated metabasite with amphibole, epidote, quartz, plagioclase, and minor titanite, chlorite, K-feldspar, and opaque minerals. Minor clasts consist of marble (calcite, minor chlorite, apatite, titanite, plagioclase), leucocratic metagranitoid (quartz, minor K-feldspar, and plagioclase and occasionally garnet), and epidosite (abundant epidote and minor titanite). Quartzite clasts are rare. The clast shape varies from rounded to angular. The texture of breccia and conglomerate is clast supported especially in CB and occasionally in DCB, whereas it is matrix supported in CSS. Matrix varies from sandy to silty and consists of the mineral phases forming the clasts.

CSS: in conglomerate the sedimentary matrix is locally foliated, and the grain size is even minor than 10 μm with albite, chlorite, and abundant interstitial hematite. Epidote crystallised in the fine-grained matrix and in micro shear zones. Locally hematite-bearing stylolites define S1 foliation and mark clast boundaries that are parallel to S1; here chlorite, albite, and epidote grains show shape preferred orientation parallel to the stylolitic cleavage. Veins intersect clasts, matrix, and stylolite (Figure 5a) and are filled by calcite. Calcite forms inequigranular aggregates, and in places twinned crystals with SPO at high angle with the veins. In addition to calcite, locally veins contain albite and minor K-feldspar and hematite. Calcite veins, with a micro-crystalline leucocratic film developed along vein walls, intersect veins filled by coarse-grained calcite and fine-grained epidote.

DCB: here locally leucocratic meta-granitoid and metabasite clasts show interlobate contacts that indicate dissolution (Figure 5b). In places the conglomerate has calcite cement. Zoned calcite crystals and coarse-grained euhedral inequigranular polygonal aggregates in cement indicate recrystallization (Figure 5c). Calcite also shows thick straight twinning. Hematite and calcite are interstitial between detrital grains and locally coarse-grained euhedral quartz crystals are associated with interstitial calcite.

In corona textures, prismatic pumpellyite is radial with respect to the clast surfaces (Figure 5d, 5e) and generally associated with Fe-epidote. Here prehnite forms scattered crystals with irregular grain boundaries that are included in coarse-grained euhedral calcite (Figure 5e). Blue amphibole rims the detrital amphibole and is in contact with calcite (Figure 5f).

Veins filled by calcite, quartz, and minor epidote intersect the clast-supported conglomerate and are intersected by thicker calcite veins that contain coarse-grained crystals and minor quartz surrounded by fine-grained calcite, which also includes host rock fragments. Straight twinning lamellae characterise calcite in this last group of veins. Cataclastic bands that intersect these veins are characterised by fragments as small as 10 μm and in turn sealed by millimetre-thick calcite veins.

Bedding in hematitic sandstone and siltstone is marked by different grain size of detrital amphibole, opaque minerals, plagioclase, epidote, quartz, and titanite. Calcite forms both detrital and interstitial grains. Locally also chlorite is interstitial to detrital grains.

Chlorite and quartz-bearing shear zones locally offset the bedding (Figure 6a), which is also intersected by veins and cataclastic bands. In the veins, chlorite is randomly oriented but, if associated with quartz, forms inequigranular aggregates with crystals at high angle to the vein walls. These veins also intersect S1 stylolitic cleavage.

In mafic siltstone, calcite and quartz-bearing veins are cut by calcite veins. Veins are filled by coarse-grained polygonal mineral aggregates with calcite crystals usually twinned. Rocks are chloritised close to the vein boundaries.

FS: fossiliferous schists are rich in carbonatic bioclasts consisting of centimetre- to decimetre-sized articulated brachiopods (Gigantoproductini), foraminifera, crinoids, and rare bryozoa with calcite shell. S1 foliation is at high angle to gently bent brachiopod shell, which are locally boudinaged with boudin necks filled by calcite and minor quartz, and at low angle with respect to S1. Geometric relationships between boudin necks and S1 suggest that boudinage predates foliation development. S1 is a wriggly to stylolitic foliation marked by opaque minerals (Figure 6b) and SPO of micrometre-sized calcite, chlorite, plagioclase, and quartz grains. Framboidal pyrite fills also veins with quartz and calcite and occurs in the rock matrix (Figure 6c). Bioclasts are elongated and dissolved along S1 (Figure 6b) or along mutual margins (Figure 6d) and shows shape preferred orientation parallel to S1. Around rare detrital plagioclase grains, albite-bearing strain shadows developed (Figure 6c). Calcite replacing bioclast shells shows straight and thick twinning. Veins sub-orthogonal to S1 are interpreted as collectors of dissolved material.

CB: breccias contain rare sandy matrix with local carbonatic cement, possibly derived from marble clast dissolution. Locally chlorite is interstitial to detrital matrix grains and, with K-feldspar, also in cataclastic bands. Locally clasts are compenetrated with lobated margins, suggesting dissolution; rare and discontinuous films nucleated at the clast margins, intersect the newly formed interstitial minerals, and are defined by SPO of chlorite and minor K-feldspar and albite.

Veins are filled by coarse-grained calcite with straight and thick twinning. Cataclastic bands are intersected by veins filled by chlorite grains at high angle with respect to the vein walls and by K-feldspar (Figure 6e). At the triple junctions of clasts calcite, chlorite, and locally radial prehnite (Figure 6f) occur. In places pumpellyite rims detrital amphibole (Figure 6f).

Mafic sandstone consists of laterally discontinuous bedding with dominant angular detrital amphibole grains and rare cm-sized marble clasts. Some samples contain up to 1.5 mm-sized clasts of metabasite and rare quartzite. Mafic siltstone contains detrital grains mostly of quartz, epidote, amphibole, and minor plagioclase. The bedding is marked by variation of detrital grain size with opaque mineral concentrated in finer-grained beds, which contain a sedimentary lamination. Locally they are folded and intersected by the dominant S1 fabric (Figure 7a). Two pervasive vein systems intersect S0 at low angle. The older system is filled by quartz and white mica (Figure 7b) and is intersected by calcite-filled veins. These are rimmed by K-feldspar that also fills successive thinner vein sets. Between feldspar and calcite fillings, albite grains are randomly distributed as in the matrix. Besides these three vein systems, 30 μm thick veins are filled with pumpellyite, phengitic mica, chlorite, and albite (Figure 7c). Locally pumpellyite is interstitial between detrital grains.

In summary metamorphic minerals overprinting Badstub rocks are: *pumpellyite, prehnite, chlorite, albite, K-feldspar, calcite, white mica, and blue amphibole*. These minerals overgrew monomineralic and polymineralic clasts, fill successive sets of veins, and mark S1 foliation. Moreover, the carbonatic cement shows textures indicating re-crystallization and calcite twinning of type II (Burkhard 1993). These observations disclose the metamorphism recorded by the Badstub Formation rocks.

6. Mineral chemistry and metamorphism

We focus on the compositional variations of metamorphic minerals that overprint the Badstub Formation sequence (Figure 8, Supp. Table 2, and Supp. Table 3). Mineral chemical analyses have been performed on selected microstructural sites with a JEOL JXA-8200 microprobe, operating at Dipartimento di Scienze della Terra 'A. Desio' of Milano University, equipped with WDS and EDS systems; operating conditions were 5 nA and 15 kV and working distance was 11 mm. The pressure and temperature (PT) conditions recorded by metasedimentary rocks of the Badstub Formation were estimated by chlorite thermometry (Bourdelle *et al.* 2013) and thermodynamic modelling based on mineral assemblages. The compositions of selected equilibrium micro-domains were quantitatively estimated by modal analysis under the electron microscope (BSE images) and converted to mass. Phase diagrams were calculated using the Gibbs free energy minimization modelling software Theriak-Domino (de Capitani and Petrakakis 2010) and the internally consistent thermodynamic dataset "ds6.2" (Holland and Powell 2011). The following a-x models were used: amphibole (Green *et al.* 2016), epidote (Holland and Powell 1998), feldspar (Holland and Powell 2003), chlorite, garnet, prehnite, pumpellyite, and white mica (White *et al.* 2014).

6.1. Mineral chemistry data

Amphibole: detrital amphibole consists of hornblende with rare pargasite; actinolite rims detrital hornblende (Figure 8a). In DCB metamorphic amphibole consists mostly of ferro-ferri-winchite and minor riebeckite and actinolite that form coronas rimming detrital amphibole (Supp. Table 2).

Chlorite: in the clasts it consists mostly of pycnochlorite and minor ripidolite and brunsgivite (Figure 8b). Metamorphic chlorite shows generally higher Si content than detrital chlorite and in CB the composition is diabanitic. Only in FS, Si content in metamorphic chlorite is lower than in the detrital one. Chlorite aligned in micro-shear zones shows higher Si values than in the metamorphic matrix (Supp. Table 2).

Epidote: Al is higher in detrital than in metamorphic epidote (Figure 8c). In DCB, metamorphic epidote is associated with pumpellyite and shows a wider compositional range than epidote in CSS (Supp. Table 2).

Pumpellyite: in micro-veins of CB pumpellyite associated with phengitic mica, chlorite, and albite shows lower X_{Mg} than crystals in the microcrystalline matrix (Supp. Table 2). Pumpellyite overgrowing detrital amphibole, both in DCB and CB, shows intermediate X_{Mg} values (Figure 8d; Supp. Table 2).

Prehnite: in CB, prehnite with the highest and lowest Fe^{3+} values (Figure 8c, Supp. Table 2) form lamellas in the same interspace. Irregular shaped crystals enclosed in calcite indicate a crystallization from CO_2-poor fluids, predating calcite (see Wheeler *et al.* 2001).

Feldspar: detrital plagioclase has a composition variable from albite to oligoclase. Metamorphic grains on the contrary consists of albite. K-feldspar in veins and in the metamorphic matrix shows a homogeneous composition (Figure 8e).

White mica: in CB, white mica in veins (if coexisting with pumpellyite and chlorite up to 3.43 apfu of Si) shows higher phengitic content with respect to detrital and metamorphic matrix white mica in FS (Figure 8f, Supp. Table 2).

6.2. Thermodynamic modelling

Two types of equilibrium assemblages were considered for phase diagrams in distinct micro-domains: spaces between clasts in meta-conglomerate (Figure 5e) and veins in meta-siltstone (Figure 7d). The interstices between metabasite clasts in meta-conglomerate (sample MA20) are filled by equilibrium assemblage of prehnite, pumpellyite, epidote, and quartz (cfr. Figure 5e). This micro-domain was modelled in the CFMASHO system (Figure 9a). The equilibrium assemblage Prh + Pmp + Ep + Qz + H_2O (mineral abbreviations in figures 5, 6, and 7 caption) is stable between 260 °C and 310 °C and 0.25 GPa and 0.50 GPa. The stability field is confined by heulandite-in reaction at low temperature, chlorite-in at low pressure, lawsonite-in and garnet-in at high pressure and temperature, respectively.

The pumpellyite-chlorite-white mica-albite-quartz assemblage in veins in the meta-siltstone (sample MA28; Figure 7d) was modelled in the KNCFMASHO system (Figure 9b). The equilibrium assemblage Pmp + Chl + Wm + Ab + Qz + H_2O is stable for temperatures and pressures comprised between 200 and 380 °C, and 0.1 and 0.7 GPa. The stability field is constrained by heulandite-in at low temperature, prehnite-in at low pressure, amphibole-in at high pressure, and garnet-in at high temperature.

The widespread twinning type in calcite grains in veins or cement (type II = 150 - 300° C according to Burkhard 1993) is coherent with the temperatures estimated in both modelled micro-domains. Moreover, in prehnite the molar fraction of $Fe^{3+} / (Fe^{3+} + Al^{VI})$ is up to 0.2 and consistent with crystallization temperature of about 250 °C (see Wheeler *et al.* 2001).

According to amphibole phase relations (Banno *et al.* 1984), ferro-ferri-winchite with minor riebeckite and actinolite rimming detrital amphibole associated with albite, chlorite, hematite, and quartz in rock matrix suggests that the rocks of the Badstub Formation were metamorphosed at temperature lower than 400 °C and pressure at around 0.4 - 0.6 GPa. These conditions are consistent with the results of thermodynamic modelling (Figure 9, 10a). Convergence of PT estimates suggests that syn-metamorphic deformation in the metasedimentary rocks of the Badstub Formation occurred at 260 - 310 °C and 0.25 - 0.50 GPa (Figure 10a).

6.3. Thermal state of the metamorphic overprint in the Badstub Formation

Estimated metamorphic temperatures and pressures for the Badstub Formation are assessed at 260 - 310 °C and 0.25 - 0.50 GPa. These estimates are based on the metamorphic equilibrium mineral assemblages that developed in coronas and veins. Equilibrium microdomains including (1) intraclast spaces filled by quartz, pumpellyite, prehnite, and epidote in meta-conglomerate and (2) veins filled by chlorite, pumpellyite, phengitic mica, quartz, and albite in meta-siltstone have been considered for thermodynamic modelling.

In order to shrink such a large stability field and constrain the most reliable PT ratio, we consider phase compositions. Thermometry based on metamorphic chlorite from matrix, coronas, S1 foliation, and veins (10 samples, 37 analyses) results in 290 ± 50 °C, except for chlorite localised in micro-shear zones that shows lower temperature around 210 ± 70 °C (Supp. Table 2). In addition, in the pumpellyite-chlorite-white mica-albite-quartz veins, the chlorite composition is consistent with temperature of 280 ± 20 °C. In the same veins, the Si content in white mica allows tracking the 3.43 apfu Si-isopleth in the pseudosection (Figure 9b). The intersection between those constrains based on phase compositions occurs at 290 °C and 0.4 GPa and overlaps the two PT fields obtained with thermodynamic modelling (Figure 9, 10a). Therefore, these are considered the most probable conditions under which the Badstub Formation experienced metamorphism.

Although the full range of pressure would imply a depth between 9 and 18 km, considering a density of 2.8 g cm^{-3} and the pressure of 0.4 GPa, a burial of 14 km would result. From the depth of 14 km and the temperature of 290 °C a thermal state of about 20 °C km^{-1} results. This is the most likely thermal state under which the metamorphic mineral assemblages that overprinted the Badstub Formation developed.

Thus, in this work we provide the first quantitative PT estimates of the metamorphic overprint in the Carboniferous of Nötsch. The temperatures we estimated are slightly higher than those previously estimated for the Carboniferous of Nötsch (Rantitsch 1995), whereas the depth of about 14 km is markedly higher than a few kilometres of subsidence that were indirectly derived from thermal estimates combined with a supposed thermal gradient of 40 °C km^{-1} (Rantitsch 1995). Our independent quantitative PT estimates opens to new interpretations and scenarios of the tectono-metamorphic evolution within the Drauzug-Gurktal Nappe System.

7. Geodynamic modelling

7.1. Selection of the tectonic scenarios for geodynamic modelling

The thermal state assessed for the metamorphism of the Badstub Formation points to the maximum term of the range 6 - 20 °C km^{-1} derived from the pressure and temperature estimates of the Eo-Alpine metamorphic peak in the Upper Austroalpine basement nappes (Faryad and Hoinkes 2003; Schuster *et al.* 2004; Gaides *et al.* 2008; Janák *et al.* 2015; Schulz 2017; Li *et al.* 2021). A similar thermal state of ca. 18 °C km^{-1} derives from constraints on the Late Cretaceous metamorphism in the Graz Palaeozoic of the Drauzug-Gurktal Nappe System, which point to higher temperature and pressure conditions (Krenn *et al.* 2008; Schantl *et al.* 2015) than those estimated in the Badstub Formation. Conversely, the thermal state estimated for the Badstub Formation is colder than 25 - 50 °C km^{-1} derived in the Upper Austroalpine basement nappes for the Permian-Triassic metamorphism (Figure 10b) recorded during the lithospheric thinning (Stöckhert 1987; Thöni and Miller 2000; Habler and Thöni 2001; Schuster *et al.* 2001; Gaides *et al.* 2006; Tenczer *et al.* 2006; Spalla and Marotta 2007; Spalla *et al.* 2014; Schuster *et al.* 2015; Schulz 2017; Roda *et al.* 2019). As the thermal gradient is usually increasing close to the surface, rather than the Permian-Triassic extension, the thermal state we estimated for the metamorphism recorded in the Badstub Formation better agrees with lithosphere convergence and thickening (Ernst and Liou 2008; Regorda *et al.* 2020). Indeed, the metamorphic conditions experienced by the Badstub Formation are comprised between the warm subduction and the plate interior geotherms (Figure 10b) and definitely unrelated to the spreading ridge or volcanic arc geotherm, as expected for a continental rifting scenario. Therefore, we consider the Alpine convergence as responsible for the metamorphic overprint on the Badstub Formation. This interpretation is also consistent with the age of Carboniferous of Nötsch that excludes a Variscan and late Carboniferous age (Schulz 2017; Neubauer *et al.* 2022) for the metamorphism recorded in the Badstub Formation.

Palaeogeographical reconstructions of pre-Alpine times show that the Carboniferous of Nötsch formed at the western margin of the Palaeotethys embayment on the palaeo-Adria plate (Vachard *et al.* 2018; Neubauer *et al.* 2022). In Permian and Triassic times, the subduction and retreat of the Palaeotethys, led to the back-arc opening of Meliata-Hallstatt ocean, a part of the western Tethyan realm (Thöni and Jagoutz 1993; Schmid *et al.* 2004, 2008; Chang *et al.* 2020, 2022; Belak et al. 2022; Neubauer *et al.* 2022). In the Eastern Alps, Middle Triassic radiolarite strata in the Northern Calcareous Alps were envisaged as the continuation of the Meliata-Hallstatt ophiolite from the Western Carpathians (Mandl and Ondrejičová 1991). Despite remnants of the Meliata-Hallstatt ocean are clear in the Western Carpathians, in many reconstructions this ocean is considered also for the Eastern Alps, although here ophiolitic remnants are scarce (Channel and Kozur 1997) and a clear suture zone has not been identified (Froitzheim *et al.* 2008). The subsequent subduction of the Meliata-Hallstatt ocean started at the end the Triassic, according to the former reconstruction

(Kozur 1991). More recent works in the Eastern Alps and Western Carpathians asses the onset of this subduction in the Early Jurassic and the end in the Late Jurassic (Froitzheim *et al.* 1996; Faryad and Henjes-Kunst 1997; Missoni and Gawlick 2011). In the Internal Dinarides the subduction the Meliata-Hallstatt ocean happened between the Middle and Late Jurassic (Slovenec and Šegvić 2019; Belak *et al.* 2022). At the time of Meliata-Hallstatt subduction, the Penninic ocean (i.e., Alpine Tethys) was opening (Mevel *et al.* 1978; Baumgartner *et al.* 1995; Bill *et al.* 2001; Schaltegger *et al.* 2002; Stampfli *et al.* 1998; Ratschbacher *et al.* 2004; Schmid *et al.* 2008; Handy *et al.* 2010; Li *et al.* 2013; Tribuzio *et al.* 2016; Rebay *et al.* 2018; Roda *et al.* 2019; Gleißner *et al.* 2021; Nicollet *et al.* 2022). Afterward in the Eastern Alps, the subduction of the Penninic ocean below the Austroalpine Nappes was ongoing in Coniacian times (Stern and Wagreich 2013) and possibly started at ca. 110 Ma in the Albian times (Wagreich 2001) with the record of eclogitic metamorphism in the Tauren Window between 90 and 38 Ma (Ratschbacher *et al.* 2004; Kurz *et al.* 2008; Schmid *et al.* 2013).

In the evolutionary context depicted above, two main scenarios can be considered for the development of the metamorphism in the Badstub Formation and in general for the Alpine tectono-metamorphic evolution of the Upper Austroalpine basement nappes of the Eastern Alps. The first scenario accounts for the continental subduction either starting as an intracontinental subduction (Janák *et al.* 2004, 2015; Stüwe and Schuster, 2010; Vrabec *et al.* 2012; Miladinova *et al.* 2021) or a continental collision of the passive margin once the oceanic lithosphere was consumed (Thöni and Jagoutz 1993; Chang *et al.* 2020, 2022). The second scenario accounts for the ablative subduction of the Austroalpine upper plate that would have been operated by subducting oceanic lithosphere (Roda *et al.* 2012).

7.2. Setup of the thermomechanical numerical model

Form the discussions reported in paragraph 7.1, a plate convergence (i.e., Alpine convergence) is the most likely tectonic setting responsible for the metamorphic thermal state recorded in the Badstub Formation. Thus, we perform a thermo-mechanical model for a generic ocean-continent subduction followed by continental collision, which allows comparing estimated metamorphic conditions with the thermal state resulting from either ablative oceanic subduction or continental subduction. The model combines linear viscous rheology for the sub-lithospheric mantle with linear viscoplastic rheology for the whole lithosphere (Marotta *et al.* 2020; Regorda *et al.* 2021). The physics is described by the equations of continuity of conservation of momentum and of conservation of energy, which includes the extended Boussinesq approximation to account for compressibility (e.g., Christensen and Yuen 1985; Gerya 2010; Ismail-Zadeh and Tackley 2010). Numerical integration has been performed by means of the 2D finite elements code SubMar (Marotta *et al.* 2006), in a rectangular domain 1400 km wide and 700 km deep (Figure 11). The Earth's surface has been treated by means of 10 km-thick sticky-air. The characteristic compositions of lower and upper continental crust, oceanic crust, and lithospheric mantle of the upper plate have been differentiated by means of markers distributed regularly with a density of 1 marker per 0.25 km^2. The rheological weakening of the mantle wedge has been simulated by assuming a constant viscosity 10^{19} Pa·s for the serpentinised mantle (Honda and Saito 2003; Arcay et al. 2005; Gerya and Stöckhert 2006; Roda *et al.* 2010). The stability field of serpentine (Schmidt and Poli 1998) has been delimited inside the hydrated mantle wedge (see details in Regorda *et al.* 2017, 2020; Marotta *et al.* 2020). Rock properties and rheological parameters are as in Regorda et al. (2021) and here synthetised in Supp. Table 4.

The velocity boundary conditions correspond to no-slip conditions along the upper and the lower boundaries of the 2D domain and free-slip conditions along the right boundary. In addition, a velocity of 3 cm yr^{-1} has been prescribed at the bottom of the oceanic crust as already proposed as best scenario for the Alpine convergence (Roda *et al.* 2010 and references therein), and along a 45° dipping plane that extends from the trench to a depth of 100 km, to facilitate the trigger of the subduction.

The thermal boundary conditions correspond to fixed temperatures at the top (27 °C) and at the bottom (1327 °C) of the model and zero thermal flux at the vertical sidewalls. The initial thermal structure is characterised by a simple conductive thermal configuration throughout the lithosphere, with temperatures that increase linearly from the surface to the base at a depth of 80 km, and a constant temperature of 1327 °C below the lithosphere. The initial geometry of the model is shown in Figure 11. The continental and oceanic crust is 30 and 10 km thick, respectively. In this way, we simulated 62 Myr of oceanic subduction followed by 60 Myr of continental subduction. This timing may apply for either the duration of the Meliata-Hallstatt or Penninic ocean subductions (see paragraph 7.1). However, this modelling does not involve the intra-oceanic subduction that some works suggest for the closure of Meliata-Hallstatt ocean below the Vardar ocean, which eventually would had been obducted onto the continental Adria margin (Schmid *et al.* 2004, 2008; Handy *et al.* 2010; Slovenec and Šegvić 2019).

7.3. Comparison of model results

During the oceanic subduction, ablation of tectonic slices from the upper plate occurs with a consequent syn-subduction exhumation of subducted continental slices within the orogenic wedge (Figure 12a, b, c). The exhumation is driven by the contrast of low viscosity of sediments and hydration and serpentinisation of the suprasubductive mantle wedge against the high viscosity of continental and oceanic slices. The ablation produces the bending of the upper plate with a consequent tectonic extrusion of the lithospheric mantle, which is not followed by a thermal rising in the lithosphere (as shown by the configuration of the isotherms in Figure 12). The thermal gradient affecting the subduction zone decreases from initial to mature stages, because of the cooling induced by the burial of oceanic slab. During collision the continental crust of the lower plate is subducted to depths (Figure 12d, e, f); afterward the convergence ends, and the gravitational re-equilibration begins. Therefore, the thermal gradient in the slab increases because of the radiogenic heating induced by the subducted continental crust. On the contrary, the thermal gradient in the orogenic wedge slightly decreases because of the reduction of the suprasubductive mantle flow.

The PT conditions, based on metamorphic mineral assemblages developed in the analysed Badstub Formation rocks, can be potentially achieved in the upper plate of the proposed model during different stages of the oceanic subduction starting from 15 Myr, as well as in the lower plate during the continental subduction after the ocean closure. According to the model, during the oceanic subduction the region where the PT conditions of metamorphism are achieved is within the orogenic wedge (cyan area in the shaded region of Figure 12a, b, c), where the continental crust, originally at 5 km depth, was buried at a depth between 13 and 18 km (Figure 12b; maximum depth range that satisfies the PT estimates) and then exhumed. In this way the numerical simulation lets to shrink the depth range constrained in the paragraph 6.3, being anyway consistent with the value of 14 km. The region in which the PT conditions recorded in Badstub Formation are satisfied (Figure 12a, b, c) shrinks with time because (i) the orogenic wedge becomes colder and (ii) the mantle above the subduction channel rises (i.e., tectonic extrusion of the lithospheric mantle). After the onset of the continental collision and the subsequent continental subduction, the metamorphic conditions of the Badstub Formation are no longer matched (Figure 12d, f) except for a narrow zone in the lower continental plate about 20 Myr after the onset of continental collision (Figure 12e), where metamorphic conditions are matched at a depth between 16 and 18 km.

8. Discussion

In this section we discuss the possible scenarios based on the tectonic, geodynamic, and palaeogeographical interpretations available from the literature. Without any absolute time constraint on the metamorphism overprinting the Badstub Formation, we can base our tectonic and geodynamic interpretations on the fitting between the PT conditions estimated with thermodynamic modelling and reproduced by the thermomechanical modelling. Since from the discussions in the previous chapters the plate convergence involving oceanic subduction is the reliable scenario for explaining the metamorphism in the Badstub Formation, in the following we discuss scenarios that involve both the Meliata-Hallstatt and Penninic oceans, which are considered in the literature for the evolution of the Eastern Alps. We compare the relative timing of PT condition fitting in the thermomechanical model with the timing constrains in the literature for the evolution of both oceans and concerned continental margins.

8.1. Scenarios involving continental collision

A possible scenario may imply that the whole Austroalpine domain was part of the northern margin of Meliata-Hallstatt ocean (Thöni and Jagoutz 1993; Chang *et al.* 2020). In this view the convergence would have started in the latest Triassic (Kozur 1991) or Early Jurassic (Missoni and Gawlick 2011) with the ocean plate subducting beneath the Adria plate (e.g., Chang *et al.* 2020) for a time interval of 60 to 40 Myr. After the complete consumption of the Meliata-Hallstatt lithosphere in the Late Jurassic (Kozur 1991; Faryad and Henjest-Kunst 1997; Schmid *et al.* 2004; Froitzheim *et al.* 2008) the Austroalpine passive margin collided with the Adria margin (Neubauer *et al.* 1999a). In this view, the Carboniferous of Nötsch could have stood on a thinned Austroalpine passive margin before entering in the footwall of the collisional margin (i.e., continental subduction). In the numerical model this scenario is highlighted by the fitting during continental collision (Figure 12e). Following other reconstructions, the Meliata-Hallstatt ocean formed within the present-day Upper Austroalpine basement nappes so that the Drauzug-Gurktal Nappe System was placed at its southern margin (Kurz and Fritz 2003; Schmid *et al.* 2004; Neubauer *et al.* 2022). In this case the Badstub Formation was placed in the upper plate during the continental collision. However, the numerical model does not reproduce this scenario (Figure 12) because PT conditions estimated for the Badstub Formation are not achieved in the upper plate (Figure 12d, e, f). Whatever the case, the metamorphic overprint recorded in the Badstub Formation should be related to the continental collision postdating the closure of Meliata-Hallstatt ocean that took place in the Late Jurassic. This timing is consistent with the subduction timing of continental units such as the Sieggraben unit where the eclogitic peak was recorded between 113 and 86 Ma (Chang *et al.* 2022) and the Schöckel Nappe of the Graz Palaeozoic where the epidote-amphibolite facies peak is at 119 - 112 Ma (Schantl *et al.* 2015). On the other hand, since the closure of Meliata-Hallstatt ocean is much older than the cluster of ages between 95 - 90 Ma retrieved for the Alpine high-pressure and ultrahigh-pressure metamorphic peak recorded in the Upper Austroalpine basement nappes

(Thöni and Jagoutz 1992; Thöni *et al.* 2008; Sandmann *et al.* 2016; Schulz 2017; Miladinova *et al.* 2021; Li *et al.* 2021), some papers explain the high-pressure age cluster at 95 - 90 Ma as due to an intracontinental subduction. Such subduction would had been induced by the reactivation of the Permian rift that is testified by the Saualpe and Koralpe metagabbro bodies and it is supposed to have developed west of Meliata-Hallstatt ocean (Janák *et al.* 2004, 2015; Stüwe and Schuster, 2010; Miladinova *et al.* 2021). The mechanical trigger of this intracontinental subduction would had been a gravitational instability due to a thermal thickening of the lithospheric mantle during the cooling of the rifted Adria lithosphere (Stüwe and Schuster, 2010). Although the mechanism is given, a thoughtful analysis of the thermal implication of the intracontinental subduction is not available from the literature. Indeed, the thermal state estimated for the Eo-Alpine event in the Upper Austroalpine basement nappes is also consistent with that achieved during an active oceanic subduction (Roda *et al.* 2012; Penniston-Dorland *et al.* 2018; Regorda *et al.* 2020).

8.2. Scenarios involving ablative oceanic subduction

The geodynamic evolution of convergent systems that include ablative oceanic subduction has been thoroughly analysed and described by many authors (e.g., Gerya and Stöckhert 2006; Meda *et al.* 2010; Roda *et al.* 2012; Regorda *et al.* 2017; Stern and Gerya 2018). The possibility for the subducting oceanic lithosphere of ablating slices from continental crust was postulated about 30 years ago for the Western Alps (Polino *et al.* 1990). Afterward, this hypothesis was supported by a thoroughly thermomechanical analysis of metamorphic conditions all over the Austroalpine domain (Stöckhert and Gerya 2005; Meda *et al.* 2010;

Roda *et al.* 2012). In the numerical model here presented this scenario is highlighted by the fitting with the PT estimates starting 15 Myr after the subduction onset (Figure 12b, c). In order to explain the metamorphism recorded by the Badstub Formation, the oceanic ablation of the continental crust may apply to either Meliata-Hallstatt or Penninic oceans, because the duration of their subductions (ca. 60 to 40 Myr) are comprised within the subduction time simulated in the thermomechanical model (62 Myr). In the first case the most suitable palaeogeographical scenario considers the Drauzug-Gurktal Nappe System at the southern Meliata-Hallstatt ocean margin (Kurz and Fritz 2003; Schmid *et al.* 2004, 2008; Neubauer *et al.* 2022). In this case the Badstub Formation was part of the upper plate during 60 to 40 Myr subduction and would have been dragged at depth by the Meliata-Hallstatt oceanic slab. The ablation induced by Meliata-Hallstatt oceanic slab can be consistent with radiometrical and petrological data indicating that continental material was subducted before the end of the subduction of Meliata-Hallstatt ocean in the Western Carpathians (Faryad and Henjes-Kunst 1997). Potentially the ablation may be operated also by the subduction of the Penninic ocean (Tauren Window) beneath the Austroalpine margin whose initiation may be assessed at ca. 110 Ma (Wagreich 2001). This age fits well with the ablation by the subducting Penninic slab that could have dragged the part of the Upper Austroalpine basement nappes, which record the eclogitic pressure peak at 95 - 90 Ma (see previous paragraph), whereas the collision of the European passive margin ended at ca. 33 Ma (Nagel *et al.* 2013). The duration of simulated subduction in the thermomechanical model is 62 Myr and thus includes the time interval necessary for the fitting of the PT estimates and to complete the subduction of both oceans, according to the literature cited in the previous paragraphs.

8.3 The shallow tectono-metamorphic evolution of the Badstub Formation

Either continental collision or oceanic subduction is considered for interpreting the tectonic significance of the metamorphism constrained in this work, the Badstub Formation was involved in the evolution of the orogenic wedge staked at the margin of Adria plate, but at significant shallower levels compared to the deeper tectonic systems of the Upper Austroalpine basement nappes. Within the Palaeozoic sequences of Drauzug-Gurkatal Nappe System, the Badstub Formation recorded metamorphic peak pressures lower than those recorded in the Graz Palaeozoic (Schantl *et al.* 2015) and peak temperatures comparable with those recorded under subgreeschist facies in the Gurktal Range (Rantitsch *et al.* 2020). Since during Permian-Mesozoic times about 5 km of sedimentary sequences formed above the Badstub Formation (Tollmann 1977; Rantitsch 1995), the cumulative depth of 13 - 18 km (Figure 12b) includes a tectonic burial of about 8 - 13 km. Despite during the Alpine convergence these rocks experienced a tectonic burial of 8 - 13 km, the Badstub Formation rocks should have behaved as a solidly poorly strained block. This is demonstrated by the heterogeneous development of the S1 foliation only in the fossiliferous schist and locally in sandstone and siltstone. As a result, very pristine sedimentary features are preserved and even an outstanding palaeontological record survived. In addition, in the studied section the normal stratigraphic polarity is preserved and strata dip southward of about 45° (Figure 2, inset a). Thus, the most important component of the finite deformation of the Badstub Formation rocks was a translation and tilting, whereas accumulation of plastic strain was scarce. This observation agrees with the scarce possibility of mylonite development in a low-grade metamorphic environment, as predicted by numerical modelling, which explore relationships between metamorphic environments and strain gradients in subduction systems (Regorda *et al.* 2021).

9. Conclusions

The Badstub Formation includes meta-conglomerate and -breccia and minor -sandstone, -siltstone, and fossiliferous carbonatic schists. Although it is exposed in the axial part of the Alpine belt, north of the Periadriatic Fault System, it preserves pristine sedimentary features, among which an outstanding Carboniferous fossil record. Even if sedimentary features are prominent and easily detectable at first glance, the multiscale structural analysis revealed an S1 foliation, which is pervasive in the fossiliferous carbonatic schists, veins, and different sets of fault systems, among which some are mineralised. Moreover, micro-scale analysis reveals very low-grade metamorphic assemblages in micro-veins, intraclasts spaces, coronas, and marking S1. Mineral assemblages are characterised by pumpellyite, prehnite, chlorite, phengitic mica, riebeckite, and winchite that are compatible with thermodynamic modelling revealing that the Badstub Formation re-equilibrated at 260 - 310 °C and 0.25 - 0.50 GPa. These results provide the first quantitative independent pressure constraints for the inferred temperature in the Carboniferous covers the Upper Austroalpine basement nappes south of the SEM line. In a 2D numerical thermomechanical modelling these temperature and pressure conditions demonstrate a cumulative burial (depositional and tectonic) of 13 - 18 km and are consistent with the development of the metamorphism recorded in the Badstub Formation during the Alpine convergence. According to the numerical model results this metamorphism could have been recorded either in the upper or lower continental plate, either during oceanic subduction or continental collision. For the oceanic subduction, we advocate the tectonic ablation of the upper plate by the subducting oceanic slab, either operated by the Meliata-Hallstatt or Penninic ocean. The continental collision could have been developed by continental subduction of the passive Austroalpine margin beneath Adria as a consequence of the complete closure of the Meliata-Hallstatt ocean. Whichever geodynamic interpretation, during the downward and upward tectonic path the Badstub sequence recorded scarce plastic strain and was mostly translated and tilted as a coherent block that was eventually stacked into the Alpine orogenic wedge accreted at the Adria margin. Finally, these metamorphic conditions are consistent with the Upper Austroalpine basement nappes recording the Alpine convergence under conditions that span from eclogitic to prehnite-pumpellyite facies.

Acknowledgements

Authors are grateful to three anonymous reviewers whose comments made a significant improvement of the manuscript possible. Christian Kofler (Mineral Abbau GmbH) gave access to the Jakomini quarry and approved the publication of the data. Georg Worsche (Worsche Vermessung) provided the updated georeferenced vectorial topography of the quarry. Lucia Angiolini, Curzio Malinverno, Andrea Risplendente, and Luca Corti (Milano University) helped with fossil determination, prepared the thin sections, assisted the acquisition of microprobe analyses, and helped with fieldwork, respectively. Funding by CTE_NAZPR18ISPAL_01 and PSR2021_MRODA.

Disclosure statement

The authors report there are no competing interests to declare.

References

Afonso, J.C., and Ranalli, G., 2004, Crustal and mantle strengths in continental lithosphere: is the jelly sandwich model obsolete? Tectonophysics, v. 394, p. 221-232.

Arcay, D., Tric, E., and Doin, M.-P., 2005, Numerical simulations of subduction zones. Physics of the Earth and Planetary Interiors, v. 149, p. 133-153.

Banno, S., Sakai, C., and Otsuki, M., 1984, Thermal history of the Sanbagawa metamorphic rocks. Journal of Geography (Chigaku Zasshi), v. 93, p. 515-527.

Baumgartner, P.O., Bartolini, A., Carter, E.S., Conti, M., Cortese, G., Danelian, T., De Wever, P., Dumitrică, P., Dumitrica-Jud, R., Goričan, Š., Guex, J., Hull, D.M., Kito, N., Marcucci, M., Matsuoka, A., Murchey, B., O'Dogherty, L., Savary, J., Vishnevskaya, V., Widz, D., and Yao, A., 1995, Middle Jurassic to Early Cretaceous radiolarian biochronology of Tethys based on Unitary Associations, *in* InterRad Jurassic-Cretaceous Working Group, ed., Middle Jurassic to Lower Cretaceous Radiolaria of Tethys: Occurrences, Systematics, Biochronology: Memoires de Géologie (Lausanne, Switzerland), v. 23, p. 1013-1048.

Belak, M., Slovenec, D., Kolar-Jurkovšek, T., Garašić, V., Pécskay, Z., Tibljaš, D., and Mišur, I., 2022, Low-grade metamorphic rocks of the Tethys subduction-collision zone in the Medvednica Mt. (NW Croatia). Geologica Carpathica, v. 73, p. 207-229. https://doi.org/10.31577/GeolCarp.73.3.3

Best, M.G., and Christiansen, E.H., 2001, Igneous Petrology: London, Blackwell Sciences, 729 p.

Bill, M., O'Dogherty, L., Guex, J., Baumgartner, P.O., and Masson, H., 2001, Radiolarite ages in Alpine-Mediterranean ophiolites: Constraints on the oceanic spreading and the Tethys-Atlantic connection. Geological Society of America Bulletin v. 113, p. 129-143. doi:10.1130/0016-7606(2001)113

Bourdelle, F., Parra, T., Chopin, C., and Beyssac, O., 2013, A new chlorite geothermometer for diagenetic to low-grade metamorphic conditions. Contributions to Mineralogy and Petrology, v. 165, p. 723-735.

Burkhard, M., 1993, Calcite twins, their geometry, appearance and significance as stress-strain markers and indicators of tectonic regime: a review. Journal of Structural Geology, v. 15, p. 351-368. https://doi.org/10.1016/0191-8141(93)90132-T

Chang, R., Neubauer, F., Liu, Y., Genser, J., Jin, W., Yuan, S., Guan, Q., Huang, Q., and Li, W., 2020, Subduction of a rifted passive continental margin: the Pohorje case of Eastern Alps - constraints from geochronology and geochemistry. Swiss Journal of Geosciences, v. 113, p. 14. https://doi.org/10.1186/s00015-020-00369-z.

Chang, R., Neubauer, F., Liu, Y., Genser, J., Yuan, S., Huang, Q., Li, W., and Yu, S., 2022, Protolith and metamorphic age of the Sieggraben Eclogites: Implications for the Permian to Cretaceous Wilson cycle in the Austroalpine unit. Lithos, v. 434-435, p. 106923. https://doi.org/10.1016/j.lithos.2022.106923

Cloos, M., 1993, Lithospheric buoyancy and collisional orogenesis: Subduction of oceanic plateaus, continental margins, island arcs, spreading ridges and seamounts. The Geological Society of America Bulletin, v. 105, p. 715-737. https://doi.org/10.1130/0016-7606(1993)105<0715:lbacos>2.3.co;2

Cortesogno, L., Lucchetti, G., and Spadea, P., 1984, Pumpellyite in low-grade metamorphic rocks from Ligurian and Lucanian Apennines, Maritime Alps and Calabria (Italy). Contribution to Mineralogy and Petrology, v. 85, p. 14-24.

Channell, J.E.T., and Kozur, H.W., 1997, How many oceans? Meliata, Vardar, and Pindos oceans in Mesozoic Alpine paleogeography. Geology v. 25, p. 183-186.

Chopra, P.N., and Paterson, M.S., 1981, The experimental deformation of dunite. Tectonophysics, v. 78, p. 453-73.

Christensen, U.R., and Yuen, D.A., 1985, Layered convection induced by phase transitions. Journal of Geophysical Research, v. 90, p. 10291-10300.

Crameri, F., 2018, Scientific colour-maps (3.0.4). Zenodo, doi:10.5281/zenodo.1287763

de Capitani, C., and Petrakakis, K., 2010, The computation of equilibrium assemblage diagrams with Theriak/Domino software. American Mineralogist, v. 95, p. 1006-1016.

Deutsch, A., 1988, Die frühalpidische Metamorphose in der Goldeck-Gruppe (Kärnten) - Nachweis anhand von Rb-Sr-Altersbestimmungen und Gefügebeobachtungen. Jahrbuch der Geologischen Bundesanstalt, v. 131, p. 553-562.

Dubois, J., and Diament, M., 1997, Géophysique: Paris, Masson, 212 p.

Ebner, F., Vozárová, A., Kovács, S., Kräutner, H.-G., Krstić, B., Szederkényi, T., Jamčić, D., Balen, D., Belak, M., and Trajanova, M., 2008, Devonian-Carboniferous pre-flysch and flysch environments in the Circum Pannonian Region. Geologica Carpathica, v. 59, p. 159-195.

England, P., and Thompson, A., 1984, Pressure-Temperature-time paths of regional metamorphism I. Heat transfer during the evolution of regions of thickened continental crust. Journal of Petrology, v. 25, p. 894-928. https://doi.org/10.1093/petrology/25.4.894

Ernst, W.G., 1976, Petrologic Phase Equilibria; San Francisco, Freeman and Company, 333 p.

Ernst, W.G., and Liou, J., 2008, High- and ultrahigh-pressure metamorphism: Past results and future prospects. American Mineralogist, v. 93, p. 1771-1786.

Exner, C., 1983, Zur Petrographie von Gneisgeröllen im Karbon von Nötsch (Kärnten). Jahrbuch der Geologischen Bundesanstalt, v. 126, p. 215-217.

Faryad, S.W., and Henjes-Kunst, F., 1997, Petrological and K-Ar and ^{40}Ar-^{39}Ar age constraints for the tectonothermal evolution of the high-pressure Meliata unit, Western Carpathians (Slovakia). Tectonophysics, v. 280, p. 141-156.

Faryad, S.W., and Hoinkes, G., 2003, P-T gradient of Eo-Alpine metamorphism within the Austroalpine basement units east of the Tauren Window (Austria). Mineralogy and Petrology, v. 77, p. 129-159.

Frey, M., Desmons, J., and Neubauer, F., 1999, The new metamorphic map of the Alps: introduction. Schweizerische Mineralogische und Petrographische Mitteilungen, v. 79, p. 1-4.

Froitzheim, N., Plašienka, D., and Schuster, R., 2008, Alpine tectonics of the Alps and Western Carpathians, *in* McCann, T., ed., The Geology of Central Europe Volume 2: Mesozoic and Cenozoic: Geological Society of London, p. 1141-1232.

Froitzheim, N., Schmid, S.M., and Frey, M., 1996, Mesozoic paleogeography and the timing of eclogite metamorphism in the Alps: A working hypothesis. Eclogae Geologicae Helvetiae, v. 89, p. 81-110.

Gaidies, F., Abart, R., de Capitani, C., Schuster, R., Connolly, J.A.D., and Reusser, E., 2006, Characterization of polymetamorphism in the Austroalpine basement east of the Tauern Window using garnet isopleth thermobarometry. Journal of Metamorphic Geology, v. 24, p. 451-475.

Gaidies, F., de Capitani, C., Abart, R., and Schuster, R., 2008, Prograde garnet growth along complex P-T-t paths: results from numerical experiments on polyphase garnet from the Wölz Complex (Austroalpine basement). Contributions to Mineralogy and Petrology, v. 155, p. 673-688.

Gerya, T.V., 2010, Introduction to numerical geodynamic modelling: New York, Cambridge University Press, 484 p.

Gerya, T.V., and Stöckhert, B., 2006, Two-dimensional numerical modeling of tectonic and metamorphic histories at active continental margins. International Journal of Earth Sciences (Geologische Rundschau), v. 95, p. 250-274. https://doi.org/10.1007/s00531-005-0035-9

Gerya T.V., and Yuen D.A., 2003, Characteristics-based marker-in-cell method with conservative finite-differences schemes for modeling geological flows with strongly variable transport properties. Physics of the Earth and Planetary Interior, v. 140, p. 293-318.

Gleißner, P., Franz, G., and Frei, D., 2021, Contemporaneous opening of the Alpine Tethys in the Eastern and Western Alps: constraints from a Late Jurassic gabbro intrusion age in the Glockner Nappe, Tauern Window, Austria. International

Journal of Earth Sciences, v. 110, p. 2705-2724. https://doi.org/10.1007/s00531-021-02075-z

Green, E.C.R., White, R.W., Diener, J.F.A., Powell, R., Holland, T.J.B., and Palin, R.M., 2016, Activity-composition relations for the calculation of partial melting equilibria in metabasic rocks. Journal of Metamorphic Geology, v. 34, p. 845-869.

Habler, G., and Thöni, M., 2001, Preservation of Permo-Triassic low-pressure assemblages in the Cretaceous high-pressure metamorphic Saualpe crystalline basement (Eastern Alps, Austria). Journal of Metamorphic Geology, v. 19, p. 679-697. DOI: 10.1046/j.0263-4929.2001.00338.x

Handy, M.R., Schmid, S.M., Bousquet, R., Kissling, E., and Bernoulli, D., 2010, Reconciling plate-tectonic reconstructions of Alpine Tethys with the geological-geophysical record of spreading and subduction in the Alps. Earth-Science Reviews, v. 102, p. 121-158. https://doi.org/10.1016/j.earscirev.2010.06.002

Haenel, R., Rybach, L., and Stegena, L., 1988, Handbook of Terrestrial Heat-Flow Density Determination: Dordrecht, Springer Netherlands, 486 p.

Hauke, M., Froitzheim, N., Nagel, T.J., Miladinova, I., Fassmer, K., Fonseca, R.O.C., Sprung, P., and Münker, P., 2019, Two high-pressure metamorphic events, Variscan and Alpine, dated by Lu-Hf in an eclogite complex of the Austroalpine nappes (Schobergruppe, Austria). International Journal of Earth Sciences, v. 108, p. 1317-1331. https://doi.org/10.1007/s00531-019-01708-8

Hauser, C., Anderle, N., Heinz, H., Plöchinger, B., Schmid, M.E., and Schönlaub, H.-P., 1982, Erläuterungen zu Blatt 200 Arnoldstein. Geologische Karte der Republik Österreich. Geologische Bundesanstalt.

Haüy, R.J., 1822, Traité de Minéralogie, 2nd edition: Paris, Bachelier.

Hey, M.H., 1954, A new review of chlorites: Mineralogical Magazine, v. 30, p. 277-292.

Hoinkes, G., Koller, F., Rantitsch, G., Dachs, E., Höck, V., Neubauer, F., and Schuster, R., 1999, Alpine metamorphism of the Eastern Alps. Schweizerische Mineralogische und Petrographische Mitteilungen, v. 79, p. 155-181.

Holland, T.J.B., and Powell, R., 1998, An internally consistent thermodynamic data set for phases of petrological interest. Journal of Metamorphic Geology, v. 16, p. 309-343.

Holland, T.J.B., and Powell, R., 2003, Activity-composition relations for phases in petrological calculations: an asymmetric multicomponent formulation. Contributions to Mineralogy and Petrology, v. 145, p. 492-501.

Holland, T.J.B., and Powell, R., 2011, An improved and extended internally consistent thermodynamic dataset for phases of petrological interest, involving a new equation of state for solids. Journal of Metamorphic Geology, v. 29, p. 333-383.

Honda, S., and Saito, M., 2003, Small-scale convection under the back-arc occurring in the low viscosity wedge. Earth and Planetary Science Letters, v. 216, p. 703-715.

Hubmann, B., Suttner, T.J., and Messner, F., 2006, Geologic frame of Palaeozoic reefs in Austria with special emphasis on Devonian reef-architecture of the Graz Palaeozoic. Joannea Geologie und Paläontologie, v. 8, p. 47-72.

Ismail-Zadeh, A., and Tackley, P.J., 2010, Computational Methods for Geodynamics: New York, Cambridge University Press, 332 p.

Janák, M., Froitzheim, N., Lupták, B., Vrabec, M., and Krogh Ravna, E.J., 2004, First evidence for ultrahigh-pressure metamorphism of eclogites in Pohorje, Slovenia: tracing deep continental subduction in the Eastern Alps. Tectonics, v. 23, p. TC5014.

Janák, M., Froitzheim, N., Yoshida, K., Sasinková, V., Nosko, M., Kobayashi, T., Hirajima, T., and Vrabec, M., 2015, Diamond in metasedimentary crustal rocks from Pohorje, Eastern Alps: A window to deep continental subduction. Journal of Metamorphic Geology, v. 33, p. 495-512.

Kirby, S.H., 1983, Rheology of the Lithosphere. Review of Geophysics, v. 21, p. 1459-1487.

Kozur, H., 1991, The evolution of the Meliata-Hallstatt ocean and its significance for the early evolution of the Eastern Alps and Western Carpathians. Palaeogeography, Palaeoclimatology, and Palaeoecology, v. 87, p. 109-135.

Krainer, K., 1992, Fazies, Sedimentationsprozesse und Paläogeographie im Karbon der Ost- und Südalpen. Jahrbuch der Geologischen Bundesanstalt, v. 135, p. 99-193.

Krainer, K., 1993, Late- and Post-Variscan Sediments of the Eastern and Southern Alps, *in* von Raumer, J.F., and Neubauer, F., eds., Pre-Mesozoic Geology in the Alps: Berlin, Springer, p. 537-564.

Krainer, K., and Mogessie, A., 1991, Composition and significance of resedimented amphibolite breccias and conglomerates (Badstub Formation) in the Carboniferous of Nötsch (Eastern Alps, Carinthia, Austria). Jahrbuch der Geologischen Bundesanstalt, v. 134, p. 65-81.

Krainer, K., and Vachard, D., 2002, Late Serpukhovian (Namurian A) microfacies and carbonate microfossils from the Carboniferous of Nötsch (Austria). Facies, v. 46, p. 1-26.

Krenn, K., Fritz, H., Mogessie, A., and Schaflechner, J., 2008, Late Cretaceous exhumation history of an extensional extruding wedge (Graz Paleozoic Nappe Complex, Austria). International Journal of Earth Sciences, v. 97, p. 1331-1352. http://dx.doi.org/10.1007/s00531-007-0221-z

Krenn, K., Kurz, W., Fritz, H., and Hoinkes, G., 2011, Eoalpine tectonics of the Eastern Alps: implications from the evolution of monometamorphic Austroalpine units (Schneeberg and Radenthein Complex). Swiss Journal of Geosciences, v. 104, p. 471-491. DOI 10.1007/s00015-011-0087-8

Kurz, W., and Fritz, H., 2003, Tectonometamorphic evolution of the Austroalpine Nappe Complex in the Central Eastern Alps - Consequences for the Eo-Alpine of the Eastern Alps. International Geology Review, v. 45, p. 1100-1127.

Kurz, W., Handler, R., and Bertoldi, C., 2008, Tracing the exhumation of the Eclogite Zone (Tauern Window, Eastern Alps) by $^{40}Ar/^{39}Ar$ dating of white mica in eclogites. Swiss Journal of Geosciences, v. 101, p., S191–S206. DOI 10.1007/s00015-008-1281-1

Laird, J., and Albee, L., 1981, High-pressure metamorphism in mafic schist from northern Vermont. American Journal of Science, v. 281, p. 97-126.

Lardeaux, J.-M., 2014, Deciphering orogeny: a metamorphic perspective. Examples from European Alpine and Variscan belts: Part I: Alpine metamorphism in the western Alps. A review. Bulletin de la Société Géologique de France, v. 185, p. 93-114. https://doi.org/10.2113/gssgfbull.185.2.93

Läufer, A.L., Frisch, W., Steinitz, G., and Loeschke, J., 1997, Exhumed fault-bounded Alpine blocks along the Periadriatic lineament: the Eder unit (Carnic Alps, Austria). Geologische Rundschau, v. 86, p. 612-626.

Li, B., Massonne, H.-J., Koller, F., and Zhang, J., 2021, Metapelite from the high- to ultrahigh- pressure terrane of the Eastern Alps (Pohorje Mountains, Slovenia) - New pressure, temperature and time constraints on a polymetamorphic rock. Journal of Metamorphic Geology, v. 39, p. 695-726. DOI: 10.1111/jmg.12581

Li, X.H., Faure, M., Lin, W., and Manatschal, G., 2013, New isotopic constraints on age and magma genesis of an embryonic oceanic crust: The Chenaillet Ophiolite in the Western Alps. Lithos v. 160-161, p. 283-291. doi:10.1016/j.lithos.2012.12.016

Locock, A.J., 2014, An Excel spreadsheet to classify chemical analyses of amphiboles following the IMA 2012 recommendations. Computers and Geosciences, v. 62, p. 1-11. DOI: 10.1016/j.cageo.2013.09.011

Mandl, G.W., and Ondrejičová, A., 1991, Über eine triadische Tiefwasserfazies (Radiolarite, Tonschiefer) in den Nördlichen Kalkalpen - ein Vorbericht. Jahrbuch der Geologische Bundesanstalt, v. 134, p. 309-318.

Marotta, A.M., Restelli, F., Bollino, A., Regorda, A., and Sabadini, R., 2020, The static and time-dependent signature of ocean-continent and ocean-ocean subduction:

the case studies of Sumatra and Mariana complexes. Geophysical Journal International, v. 221, p. 788-825.

Marotta, A.M., Spelta, E., and Rizzetto, C., 2006, Gravity signature of crustal subduction inferred from numerical modelling. Geophysical Journal International, v. 166, p. 923-938.

Meda, M., Marotta, A.M., and Spalla, M.I., 2010, The role of mantle hydration into the continental crust recycling in the wedge region, Geological Society, London, Special Publications, v. 332, p. 149-172.

Mevel, C., Caby, R., Kienast, J.R., 1978, Amphibolite facies conditions in the oceanic crust: example of amphibolitized flaser-gabbro and amphibolites from the Chenaillet ophiolite massif (Hautes Alpes, France). Earth and Planetary Science Letters v. 39, p. 98-108. doi:10.1016/0012-821X(78)90146-2.

Miladinova, I., Froitzheim, N., Nagel, T.J., Janák, M., Fonseca, R.O.C., Sprung, P., and Münker, C., 2021, Constraining the process of intracontinental subduction in the Austroalpine Nappes: Implications from petrology and Lu-Hf geochronology of eclogites. Journal of Metamorphic Geology, v. 40, p. 423-456.

Missoni, S., and Gawlick, H.-J., 2011, Evidence for Jurassic subduction from the Northern Calcareous Alps (Berchtesgaden; Austroalpine, Germany). International Journal of Earth Sciences, v. 100, p. 1605-1631. DOI 10.1007/s00531-010-0552-z

Nagel, T.J., Herwartz, D., Rexroth, S., Münker, C., Froitzheim, N., and Kurz, W., 2013, Lu-Hf dating, petrography, and tectonic implications of the youngest Alpine eclogites (Tauern Window, Austria). Lithos, v. 170-171, p. 179-190. http://dx.doi.org/10.1016/j.lithos.2013.02.008

Neubauer, F., Dallmeyer, R.D., and Takasu, A., 1999a, Conditions of eclogite formation and age of retrogression within the Sieggraben unit, Eastern Alps: Implications for Alpine-Carpathian tectonics. Schweizerische Mineralogische und Petrographische Mitteilungen, v. 79, p. 297-307.

Neubauer, F., Hoinkes, G., and Sassi, F.P., 1999b, Pre-Alpine metamorphism of the Eastern Alps. Schweizerische Mineralogische und Petrographische Mitteilungen, v. 79, p. 41-62.

Neubauer, F., Liu, Y., Dong, Y., Chang, R., Genser, J., and Yuan, S., 2022, Pre-Alpine tectonic evolution of the Eastern Alps: From Prototethys to Paleotethys. Earth-Science Reviews, v. 226, p. 103923. doi: 10.1016/j.earscirev.2022.103923.

Nicollet, C., Paquette, J.-L., Bruand, E., Bosse, V., and Pereira, I., 2022, Crystallisation and fast cooling of the (meta)gabbro from the Chenaillet ophiolite (Western Alps): In-situ U-Pb dating of zircon, titanite, monazite and xenotime in textural context. Lithos, https://doi.org/10.1016/j.lithos.2022.106620

Niedermayr, G., Auer, C., Bernhard, F., Blass, G., Bojar, H.-P., Brandstätter, F., Hammer, V.M.F., Hirche, T., Huber, P. A., Knobloch, G., Köller, R., Kolitsch, U., Löffler, E., Neuhold, F., Poeverlein, R., Postl, W., Prasnik, H., Pristacz, H., Schachinger, T., Strasser, M., and Walter, F., 2010, Neue Mineralfunde aus Österreich LIX. Naturwissenschaftlicher Verein für Kärnten, Austria, Carinthia, v. II,(200/120), p. 199-260.

Niedermayr, G., Mullis, J., Niedermayr, E., and Schramm, J.-M., 1984, Zur Anchimetamorphose permoskythischer Sedimentgesteine im westlichen Drauzug, Kärnten-Osttirol (Österreich). Geologische Rundschau, v. 73, p. 207-221.

Penniston-Dorland, S.C., Kohn, M.J., and Piccoli, P.M., 2018, A mélange of subduction temperatures: Evidence from Zr-in-rutile thermometry for strengthening of the subduction interface. Earth and Planetary Science Letters, v. 482, p. 525-535. https://doi.org/10.1016/j.epsl.2017.11.005

Piller, W.E., 2014, The lithostratigraphic units of the Austrian stratigraphical chart 2004 (sedimentary successions). Vol. 1. The Paleozoic Era(them). 2nd edition. Abhandlungen der Geologischen Bundesanstalt, v. 66, p. 1-136.

Polino, R., Dal Piaz, G.V., and Gosso, G., 1990, Tectonic erosion at the Adria margin and accretionary processes for the Cretaceous orogeny of the Alps. Mémoires de la Société Géologique de France, v. 156, p. 345-367.

Ranalli, G., and Murphy, D.C., 1987, Rheological stratification of the lithosphere. Tectonophysics, v. 132, p. 281-295.

Rantitsch, G., 1995, Niedrigstragradige Metamorphose im Karbon von Nötsch (Österreich). Jahrbuch der Geologische Bundesanstalt, v. 138, p. 433-440.

Rantitsch, G. 1997, Thermal history of the Carnic Alps (Southern Alps, Austria) and its palaeogeographic implications. Tectonophysics, v. 272, p. 213-232.

Rantitsch, G., Iglseder, C., Schuster, R., Hollinetz, M.S., Huet, B., and Werdenich, M., 2020, Organic metamorphism as a key for reconstructing tectonic processes: a case study from the Austroalpine unit (Eastern Alps). International Journal of Earth Sciences, v. 109, p. 2235-2253.

Rantitsch, G., Rainer, T., and Russegger B., 2000, Niedrigstgradige Metamorphose im Karbon der Südalpen (Kernten, Österreich). Carinthia, v. II,(190, 110), p. 537-542.

Rantitsch, G., and Russegger, B., 2000, Thrust-related very low grade metamorphism within the Gurktal Nappe Complex (Eastern Alps). Jahrbuch der Geologische Bundesanstalt, v. 142, p. 219-225.

Ratschbacher, L., Dingeldey, C., Miller, C., Hacker, B.R., McWilliams, M.O., 2004, Formation, subduction, and exhumation of Penninic oceanic crust in the Eastern Alps: time constraints from ^{40}Ar/^{39}Ar geochronology. Tectonophysics, v. 394, p. 155-170. doi:10.1016/j.tecto.2004.08.003

Rebay, G., Zanoni, D., Langone, A., Luoni, P., Tiepolo, M., and Spalla, M.I., 2018, Dating of ultramafic rocks from the Western Alps ophiolites discloses Late Cretaceous subduction ages in the Zermatt-Saas Zone. Geological Magazine, v. 155, p. 298-315. https://doi.org/10.1017/S0016756817000334

Regorda, A., Lardeaux, J.-M., Roda, M., Marotta, A.M., and Spalla, M.I., 2020, How many subductions in the Variscan orogeny? Insights from numerical models. Geoscience Frontiers, v. 11, p. 1025-1052. https://doi.org/10.1016/j.gsf.2019.10.005

Regorda, A., Roda, M., Marotta, A.M., and Spalla, M.I., 2017, 2-D numerical study of hydrated wedge dynamics from subduction to post-collisional phases. Geophysical Journal International, v. 211, p. 952-978. https://doi.org/10.1093/gji/ggx336

Regorda, A., Spalla, M.I., Roda, M., Lardeaux, J.-M., and Marotta, A.M., 2021, Metamorphic Facies and Deformation Fabrics Diagnostic of Subduction: Insights From 2D Numerical Models. Geochemistry, Geophysics, Geosystems, v. 22. https://doi.org/10.1029/2021GC009899

Roda, M., Marotta, A.M., and Spalla, M.I., 2010, Numerical simulations of an ocean-continent convergent system: Influence of subduction geometry and mantle wedge hydration on crustal recycling. Geochemistry, Geophysics, Geosystems, v. 11, p. 1-21.

Roda, M., Marotta, A.M., and Spalla, M.I., 2011, The effects of the overriding plate thermal state on the slab dip in an ocean-continent subduction system. Comptes Rendus Geoscience, v. 343, p. 323-330.

Roda, M., Regorda, A., Spalla, M.I., and Marotta, A.M., 2019, What drives Alpine Tethys opening? Clues from the review of geological data and model predictions. Geological Journal, v. 54, p. 2646-2664. https://doi.org/10.1002/gj.3316

Roda, M., Spalla, M.I., and Marotta, A.M., 2012, Integration of natural data within a numerical model of ablative subduction: a possible interpretation for the Alpine dynamics of the Austroalpine crust. Journal of Metamorphic Geology, v. 30, p. 973-996. https://doi.org/10.1111/jmg.12000

Rode, S., Rösel, D., and Schulz, B., 2012, Constraints on the Variscan P-T evolution by EMP Th-U-Pb monazite dating in the polymetamorphic Austroalpine Oetztal-

Stubai basement (Eastern Alps). Zeitschrift der Deutschen Gesellschaft fur Geowissenschaften, v. 163, p. 43-68.

Sandmann, S., Herwartz, D., Kirst, F., Froitzheim, N., Nagel, T.J., Fonseca, R.O.C., Münker, C., and Janák, M., 2016, Timing of eclogite-facies metamorphism of mafic and ultramafic rocks from the Pohorje Mountains (Eastern Alps, Slovenia) based on Lu-Hf garnet geochronometry. Lithos, v. 262, p. 576-585. https://doi.org/10.1016/j.lithos.2016.08.002

Schaltegger, U., Desmurs, L., Manatschal, G., Müntener, O., Meier, M., Frank, M., and Bernoulli, D., 2002, The transition from rifting to sea-floor spreading within a magma-poor rifted margin: field and isotopic constraints. Terra Nova, v. 14, p. 156-162.

Schantl, P., Schuster, R., Krenn, K., and Hoinkes, G., 2015, Polyphase metamorphism at the southeastern margin of the Graz Paleozoic and the underlying Austroalpine basement units. Austrian Journal of Earth Sciences, v. 108, p. 219-238. DOI: 10.17738/ajes.2015.0023

Schmid, S.M., Bernoulli, D., Fügenschuh, B., Manteco, L., Schefer, S., Schuster, R., Tischler, M, and Ustaszewski, K., 2008, The Alpine-Carpathian-Dinaridic orogenic system: correlation and evolution of tectonic units. Swiss Journal of Geosciences, v. 101, p. 139-183. DOI 10.1007/s00015-008-1247-3

Schmid, S.M., Fügenschuh, B., Kissling, E., and Schuster, R., 2004, Tectonic map and overall architecture of the Alpine orogen. Eclogae Geologicae Helvetiae, v. 97, p. 93-117. DOI 10.1007/s00015-004-1113-x

Schmid, S.M., Scharf, A., Handy, M.R., and Rosenberg, C.L., 2013, The Tauern Window (Eastern Alps, Austria): a new tectonic map, with cross-sections and a tectonometamorphic synthesis. Swiss Journal of Geosciences, v. 106, p. 1-32. DOI 10.1007/s00015-013-0123-y

Schmidt, M.W., and Poli, S., 1998, Experimentally based water budgets for dehydrating slabs and consequences for arc magma generation. Earth and Planetary Science Letters, v. 163, p. 361-379.

Schönlaub, H.-P., 1985, Das Karbon von Nötsch und sein Rahmen. Jahrbuch der Geologischen Bundesanstalt, v., 127, p. 673-692.

Schönlaub, H.-P., and Heinisch, H., 1994, The classic fossiliferous Palaeozoic units of the Eastern and Southern Alps, *in* von Raumer, J.F., and Neubauer, F., eds., Pre-Mesozoic Geology in the Alps: Berlin, Springer, p. 395-422.

Schorn, S., Hartnady, M.I.H., Diener, J.F.A., Clark, C., and Harris, C., 2021, H_2O-fluxed melting of eclogite during exhumation: an example from the eclogite type-locality, Eastern Alps (Austria). Lithos, v. 390-391, p. 106-118, https://doi.org/10.1016/j.lithos.2021.106118.

Schraut, G., 1999, Paläofaunistische Untersuchungen aus dem Unter-Karbon von Nötsch (Kärten, Österreich), Teil 2: Cephalopoda (Nautoloidea, Ammonoidea), Crustacea (Phyllocarida), Echinoidea. Jahrbuch der Geologischen Bundesanstalt, v., 141, p. 503-517.

Schulz, B., 2017, Polymetamorphism in garnet micaschists of the Saualpe Eclogite Unit (Eastern Alps, Austria), resolved by automated SEM methods and EMP–Th–U–Pb monazite dating. Journal of Metamorphic Geology, v. 35, p. 141-163. doi:10.1111/jmg.12224

Schuster, R., Koller, F., Hoeck, V., Hoinkes, G., and Bousquet, R., 2004, Explanatory notes to the map: Metamorphic structures of the Alps metamorphic evolution of the eastern Alps. Mitteilungen der Östereichischen Mineralogischen Gesellschaft, v. 149, p. 175-199.

Schuster, R., Scharbert, S., Abart, R., and Frank, W., 2001, Permo-Triassic extension and related HT/ LP metamorphism in the Austroalpine-Southalpine realm. Mitteilungen der Gesellschaft der Geologie und Bergbaustudenten Österreichs, v. 45, p. 111-141.

Schuster, R., and Stüwe, K., 2008, Permian metamorphic event in the Alps. Geology, v. 36, p. 603-606. doi: 10.1130/G24703A.1

Schuster, R., and Stüwe, K., 2022, Geological and Tectonic Setting of Austria, *in* Embleton-Hamann, C., ed., Landscapes and Landforms of Austria, Springer Cham, p. 3-26.

Schuster, R., Tropper, P., Krenn, E., Finger, F., Frank, W., and Philippitsch, R., 2015, Prograde Permo-Triassic metamorphic HT/LP assemblages from the Austroalpine Jenig Complex (Carinthia, Austria). Austrian Journal of Earth Sciences, v. 108, p. 73-90.

Sieber, R., 1972, Zur Paläoökologie der unterkarbonischen Bivalvenfauna von Nötsch (S Bleiberg) in Kärnten. Annalen des Naturhistorischen Museums in Wien, v. 76, p. 491-498.

Slovenec, D., and Šegvić, B., 2019, Boninite volcanic rocks from the mélange of NW Dinaric-Vardar ophiolite zone (Mt. Medvednica, Croatia) - record of Middle to Late Jurassic arc-forearc system in the Tethyan subduction factory. Mineralogy and Petrology, v. 113, p. 17-37. https://doi.org/10.1007/s00710-018-0637-0

Spalla, M.I., and Marotta, A.M., 2007, P-T evolutions vs. numerical modelling: a key to unravel the Paleozoic to Early-Mesozoic tectonic evolution of the Alpine area. Periodico di Mineralogia, v. 76, p. 267-308. doi:10.2451/2007PM0029

Spalla, M.I., Zanoni, D., Marotta, A.M., Rebay, G., Roda, M., Zucali, M., and Gosso, G., 2014, The transition from Variscan collision to continental break-up in the Alps: insights from the comparison between natural data and numerical model predictions. Geological Society, London, Special Publications, v. 405, p. 363-400. https://doi.org/10.1144/SP405.11

Stampfli, G., Mosar, J., Marquer, D., Marchant, R., Baudin, T., and Borel, G., 1998, Subduction and obduction processes in the Swiss Alps. Tectonophysics, v. 296, p. 159-204. doi:10.1016/S0040-1951(98)00142-5

Stern, G., and Wagreich, M., 2013, Provenance of the Upper Cretaceous to Eocene Gosau Group around and beneath the Vienna Basin (Austria and Slovakia). Swiss Journal of Geosciences, v. 106, p. 505-527. DOI 10.1007/s00015-013-0150-8

Stern, R.J., and Gerya T.V., 2018, Subduction initiation in nature and models: A review. Tectonophysics, v. 746, p. 173-198.

Stöckhert, B., 1987, Das Uttenheimer Pegmatitfeld (Ostalpines Altkristallin, Südtirol) Genese und alpine Überprägung. Erlanger Geologische Abhandlungen, v. 114, p. 83-106.

Stöckhert, B., and Gerya, T.V., 2005, Pre-collisional high pressure metamorphism and nappe tectonics at active continental margins: a numerical simulation. Terra Nova, v. 17, p. 102-110. https://doi.org/10.1111/j.1365-3121.2004.00589.x

Stüwe, K., and Schuster, R., 2010, Initiation of subduction in the Alps: Continent or ocean? Geology, v. 38, p. 175-178. doi: 10.1130/G30528.1

Tenczer, V., Powell, R. and Stüwe, K., 2006, Evolution of H_2O content in a polymetamorphic terrane: the Plattengneiss Shear Zone (Koralpe, Austria). Journal of Metamorphic Geology, v. 24, p. 281-295.

Thöni, M., and Jagoutz, E., 1992, Some new aspects of dating eclogites in orogenic belts: Sm-Nd, Rb-Sr, and Pb-Pb isotopic results from the Austroalpine Saualpe and Koralpe type-locality (Carinthia/Styria, southeastern Austria). Geochimica et Cosmochimica Acta, v. 56, p. 347-368.

Thöni, M., and Jagoutz, E., 1993, Isotopic constraints for eo-Alpine high-P metamorphism in the Austroalpine nappes of the Eastern Alps: bearing on Alpine orogenesis. Schweizerische Mineralogische und Petrographische Mitteilungen, v. 73, p. 177-189.

Thöni, M., and Miller, C., 2000, Permo-Triassic pegmatites in the eo-Alpine eclogite-facies Koralpe complex, Austria: age and magma source constraints from mineral chemical Rb-Sr and Sm-Nd isotope data. Schweizerische Mineralogische und Petrographische Mitteilungen, v. 80, p. 169-186.

Thöni, M., Miller, C., Blichert-Toft, J., Whitehouse, M.J., Konzett, J., and Zanetti, A., 2008, Timing of high-pressure metamorphism and exhumation of the eclogite type-locality (Kupplerbrunn-Prickler Halt, Saualpe, south-eastern Austria): constraints from correlations of the Sm-Nd, Lu-Hf, U-Pb and Rb-Sr isotopic systems. Journal of Metamorphic Geology, v. 26, p. 561-581. doi:10.1111/j.1525-1314.2008.00778.x

Tollmann, A., 1977, Geologie von Österreich. Band 1. Die Zentralalpen. Deuticke Wien, 766 pp.

Tribuzio, R., Garzetti, F., Corfu, F., Tiepolo, M., and Renna, M.R., 2016, U-Pb zircon geochronology of the Ligurian ophiolites (Northern Apennine, Italy): Implications for continental breakup to slow seafloor spreading. Tectonophysics, v. 666, p. 220-243. doi:10.1016/j.tecto.2015.10.024

Vachard, D., Krainer, K., and Schönlaub, H.-P., 2018, Lower Serpukhovian (Steshevian) foraminifers and algae from exotic limestone clasts of Nötsch (Eastern Alps, Austria). Geobios, v. 51, p. 75-100.

Vignaroli, G., Belardi, G., and Serracino, M., 2013, Multi-scale geological evaluation for quarrying activities in ophiolitic rocks: implications for asbestos-related legislation. Bulletin of Engineering Geology and Environment, v. 72, p. 285-302. DOI 10.1007/s10064-013-0475-6.

Vrabec, M., Janák, M., Froitzheim, N., and De Hoog, J.C.M., 2012, Phase relations during peak metamorphism and decompression of the UHP kyanite eclogites, Pohorje Mountains (Eastern Alps, Slovenia). Lithos, v. 144, p. 40-55.

Wagreich, M., 2001, A 400-km-long piggyback basin (Upper Aptian - Lower Cenomanian) in the Eastern Alps. Terra Nova, v. 13, p. 401-406.

Wheeler, R.S., Browne, R.L., and Rodges, K.A., 2001, Iron-rich and iron-poor prehnites from the Way Linggo epithermal Au-Ag deposit, southwest Sumatra, and the Heber geothermal field, California. Mineralogical Magazine, v. 65, p. 397-406.

White, R.W., Powell, R., Holland, T.J.B., Johnson, T.E., and Green, E.C.R., 2014, New mineral activity-composition relations for thermodynamic calculations in metapelitic systems. Journal of Metamorphic Geology, v. 32, p. 261-286.

Figure captions

Figure 1. a) Geological sketch map of the Eastern Alps that highlights the nappe systems within the Austroalpine domain (modified after Schmid *et al.* 2004); in the inset the location of Eastern Alps (red rectangle) within the national borders of central southern Europe; SAM = Southern border of Alpine metamorphism (Hoinkes *et al.* 1999; Schuster *et al.* 2004); b) Geological sketch map of the Carboniferous of Nötsch with regional fault systems, modified after Schönlaub (1985), Krainer and Mogessie (1991), and Vachard et al. (2018). Ages are from Piller (2014).

Figure 2. Geological map of the Jakomini quarry mapped in mid-December 2017 and N-S geological cross-section. Worsche Vermessung provided the base map. Pale colours indicate the inaccessible parts of the quarry during the fieldwork. In the inset equal area stereographic projection, lower hemisphere, with number of orientation data (N): a) pole to plane of bedding (S0) and S1 foliation; b) planes of fault surface (FP) and linear kinematic indicators (FL).

Figure 3. a) Metabasic clasts embodied in the red matrix intersected by fracture systems in CSS. b) Decimetre-thick conglomeratic breccia bed with angular marble clasts and minor metabasic clasts, in CSS. c) Angular to subrounded metabasic and marble clasts in the mafic conglomerate of DCB. d) Decimetre-thick red sandstone and siltstone beds within the mafic conglomerate of DCB. e) Centimetre-thick layer of conglomerate in DCB that is cemented by calcite. f) Boundary between brachiopod rich shale strata of sector FS and the greenish sandstone of DCB. g) Centimetre-thick mafic siltstone and pelite beds (white arrows) marking the boundary of conglomerate beds in CB. h) Rounded metabasic and marble clasts in the conglomerate of CB.

Figure 4. a) Bedded red conglomerate, sandstone, and siltstone of CSS that are intersected by cataclastic bands and fracture systems. b) Decimetre-thick beds of

siltstone and sandstone of CSS with S1 foliation recorded only in siltstone; c) Brachiopod rich shale that records the S1 foliation intersecting the bedding (S0) in FS; coin for scale. d) Calcite veins in a cm-thick shear zone deflecting S1 foliation in fossiliferous carbonatic schist of FS; ink marker for scale. e) Fault surface with calcite fibres in the schist of FS. f) Centimetre-thick vein filled by epidote and chlorite in the conglomeratic breccia of CB.

Figure 5. a) Sample MA17, CSS, meta-conglomerate with sub-rounded to angular clasts surrounded by hematite matrix and intersected by calcite veins; plane polarised light; b) Sample MA12, DCB, meta-conglomerate with dominant rounded metabasic clasts in recrystallised calcite cement; plane polarised light; c) Sample MA12, DCB, detail on twinning in polygonal calcite around a foliated metabasic clast; plane polarised light; d) Sample MA20, DCB, interstitial coarse-grained quartz and calcite crystals with pumpellyite radial to the clast surface; plane polarised light; e) Sample MA20, DCB, close up of previous photo with pumpellyite (Pmp) crystals radial to the clast surface and associated with epidote (Ep) in contact with euhedral coarse-grained quartz (Qz) crystal; prehnite (Prh) is enclosed in calcite (Cc); backscattered electron image; f) Sample MA23, sector DCB, portion of brecciated amphibolite clast with amphibole (Amp) from the clast with a rim of coronitic blue amphibole (light grey) in contact with calcite (Cc); also chlorite (Chl) partly replace amphibole; backscattered electron image. Sample location is shown in Figure 2.

Figure 6. a) Sample MA25, DCB, meta-sandstone, sedimentary lamination intersected by quartz and chlorite veins; crossed polars; b) Sample MA10, FS, fossiliferous schist with stylolitic S1 foliation with brachiopod spines (L. Angiolini pers.com.) partly dissolved; plane polarised light; c) S1 marked by shape preferred orientation of chlorite

(Chl), albite (Ab), and calcite (Cc); euhedral pyrite (Py) is scattered along the foliation; backscattered electron image; d) Sample MA7, FS, fossiliferous schist rich in crinoids that are partly dissolved along stylolitic S1 foliation that is intersected by sub-orthogonal calcite veins that collect the dissolved carbonate; plane polarised light; e) Sample MA33, meta-conglomerate of DC overprinted by a fault breccia, which is the finer-grained material (darker), intersected by chlorite veins; plane polarised light; f) Sample MA2, conglomerate of DC, prehnite (Prh) at the triple junction of leucocratic metagranitoid and amphibolite clasts; between prehnite a detrital titanite (Ttn) crystals is included; pumpellyite (Pmp) formed at the rim of amphibole (Amp) included in clasts; backscattered electron image. Sample location is shown in Figure 2.

Figure 7. a) Sample MA28 meta-siltstone of CB in which the original stratigraphy (S0) is poorly preserved and S1 is the dominant fabric; S1 is intersected by subsequent generation of veins; plane polarised light; b) Sample MA28 meta-siltstone of CB; vein filled by white mica (Wm), quartz (Qz), and minor chlorite (Chl); close to the vein pumpellyite (Pmp) formed in the rock matrix; backscattered electron image; c) Sample MA28 meta-siltstone of CB; microscopic vein filled by pumpellyite (Pmp), albite (Ab), white mica (Wm), and chlorite (Chl); backscattered electron image. Sample location is shown in Figure 2.

Figure 8. Composition of metamorphic minerals that overprint the sequences in the four zones. Fields delimitate the composition of detrital minerals (in clasts and detrital grains). a) Classification diagram for amphibole (Laird and Albee, 1981) with formula calculated on 23 oxygen atoms, according to Locock (2014); Gl = glaucophane; Ktp = katophorite; Brs = barroisite; Prg = pargasite; Sdg = sadaganaite; Ts = tschermakite; Act = actinolite; Ed = edenite; Wnc = winchite; b) Classification diagram for chlorite (Hey

1954) with formula calculated on 14 oxygen atoms, according to Bourdelle et al. (2013); c) Composition of epidote and prehnite with Fe^{3+} estimated on charge balance and formula based on 12.5 oxygen atoms and 14 cations, respectively; d) Composition of pumpellyite with formula based on 16 cations according to Cortesogno et al. (1984); e) Composition of feldspar with formula based on 8 oxygen atoms; f) Composition of white mica with formula based on 11 oxygen atoms.

Figure 9. a) CFMASHO phase diagram that models the stability field of mineralised interstices between metabasite clasts in MA20 meta-conglomerate. The bulk composition determined on the modal amount of metamorphic minerals is reported at the top of the diagram. The Pre + Pmp + Ep + Qz + H_2O stability field is coloured in green. Univariant lines are double thickness. b) KNCFMASHO phase diagram that models the stability field of mineralised veins in MA28 meta-siltite. The bulk composition determined on the modal amount of metamorphic minerals is reported at the top of the diagram. The Pmp + Chl + Wm + Ab + Qz + H_2O stability field is coloured in light blue. Si-in white mica isopleths (apfu) are tracked in dark blue. Small fields were not labelled. Univariant lines are double thickness.

Figure 10. a) Summary of PT conditions determined for the Badstub Formation metasedimentary rocks with different thermobarometric methods. Stability fields of actinolite (Act), winchite (Wnc), magnesioriebeckite (Mrb), barroisite (Brs), and hornblende (Hbl) are from Banno et al. (1984). The results converge to T = 260 - 310 °C and P = 0.25 - 0.50 GPa. b) Metamorphic conditions determined for the Badstub Formation (cyan rectangle) compared with the petrogenetic PT grid (modified after Ernst 1976) with black-thick lines representing geothermal gradients traditionally associated to arc regions (1), plate interior (2), warm subduction zones (3) and cold

subduction zones (4), according to Cloos (1993), and red-thick lines representing stable (V_0) and relaxed ($V\infty$) geotherms, according to England and Thompson (1984). Labels of metamorphic facies: Z: zeolite; PP: prehnite-pumpellyite; BS: blueschist; GS: greenschist; EA: epidote amphibolite; A: amphibolite; E: eclogite; G: granulite. The pink area represents the PT field of Permian-Triassic metamorphic imprints recorded in the continental crustal units of the Alps (Roda *et al.* 2019 and references therein).

Figure 11. Model setup. The model domain is 1400 km wide and 700 km deep. The Earth's surface has been treated by means of a 10 km-thick sticky-air. The characteristic compositions of lower and upper continental crust, oceanic crust, and lithospheric mantle of the upper plate have been differentiated by means of markers distributed regularly with a density of 1 marker per 0.25 km^2. The velocity boundary conditions correspond to no-slip conditions along the upper and the lower boundaries of the 2D domain and free-slip conditions along the right boundary. In addition, a velocity of 3 cm yr^{-1} has been prescribed at the bottom of the oceanic crust and along a 45° dipping plane that extends from the trench to a depth of 100 km, to facilitate the trigger of the subduction. The thermal boundary conditions correspond to fixed temperatures at the top (27 °C = 300 K) and at the bottom (1327 °C = 1600 K) of the model and zero thermal flux at the vertical sidewalls. The initial thermal structure is characterised by a simple conductive thermal configuration throughout the lithosphere, with temperatures that increase linearly from the surface to its base located at a depth of 80 km, and a constant temperature of 1327 °C below the lithosphere.

Figure 12. Thermal field of the model for 122 Myr of convergence, from subduction (a, b, c) to continental collision and gravitational requilibration (d, e, f). Black solid lines represent crustal boundaries (OC = oceanic crust; CC = continental crust; S = trench

sediments). Isotherms 260 and 310 °C are reported as white dashed lines. The orogenic wedge is enclosed in the shaded area. The PT conditions inferred for the metamorphism of Badstub Formation (T = 260 - 310 °C and P = 0.25 - 0.5 GPa) in the continental crust are indicated by cyan area. In the upper plate these conditions are confined within the orogenic wedge where tectonic burial occurs, whereas in the lower plate these conditions are constrained by 5 km of sedimentary sequences above the Badstub Formation indicated with the black dashed line. Model results indicate that the metamorphic conditions recorded by the Badstub Formation are potentially achieved in the upper plate during oceanic subduction or in the lower plate during continental subduction at a depth of 13 - 18 km and 16 - 18 km, respectively. Colour map after Crameri (2018).

Supplemental online material

Supp. Table 1. Summary of rock types, sedimentary environments, and ages of the Carboniferous of Nötsch (Krainer and Mogessie 1991; Krainer 1992; Schönlaub and Heinisch 1994; Krainer and Vachard 2002; Hubmann *et al.* 2006; Ebner *et al.* 2008; Vachard *et al.* 2018).

Supp. Table 2. Summary of mineral composition shown by means of average and standard deviation or maximum and minimum values of cations from the stoichiometric formulae. In brackets the quarry sector is indicated. NC = not calculated, NS = not shown.

Supp. Table 3: excel multi-sheet file that contains selected mineral chemical analyses with stoichiometric formulae.

Supp. Table 4. Thermal and rheological parameters. References: (1) Ranalli and Murphy (1987); (2) Haenel et al. (1988); (3) Dubois and Diament (1997); (4) Best and Christiansen (2001); (5) Gerya and Yuen (2003); (6) Afonso and Ranalli (2004); (7) Gerya and Stöckhert (2006); (8) Roda et al. (2012); (9) Kirby (1983); (10) Chopra and Peterson (1981); (11) Schmidt and Poli (1998); (12) Roda et al. (2011).

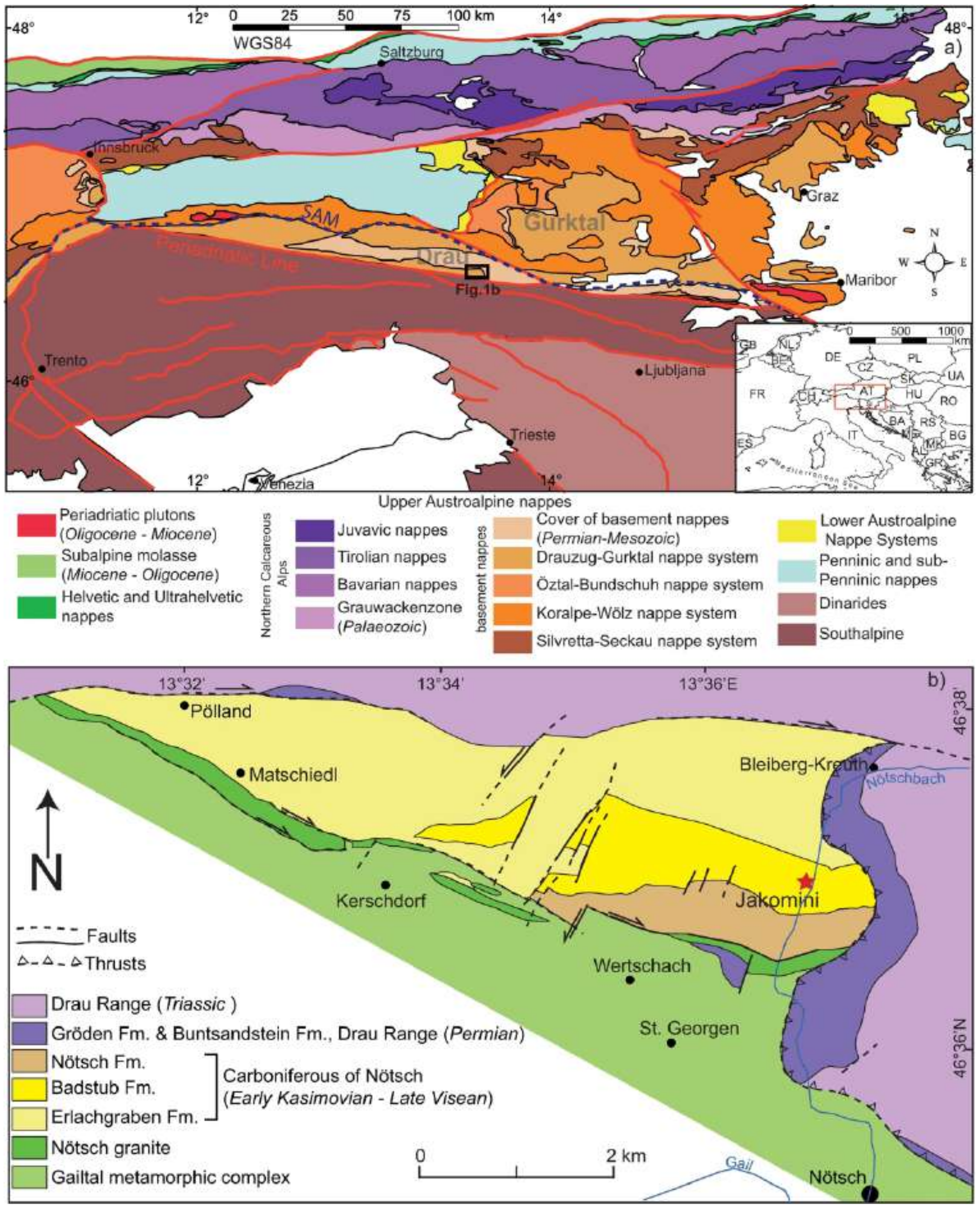

Figure 1. a) Geological sketch map of the Eastern Alps that highlights the nappe systems within the Austroalpine domain (modified after Schmid et al. 2004); in the inset the location of Eastern Alps (red rectangle) within the national borders of central southern Europe; SAM = Southern border of Alpine metamorphism (Hoinkes et al. 1999; Schuster et al. 2004); b) Geological sketch map of the Carboniferous of Nötsch with regional fault systems, modified after Schönlaub (1985), Krainer and Mogessie (1991), and Vachard et al. (2018). Ages are from Piller (2014).

203x250mm (300 x 300 DPI)

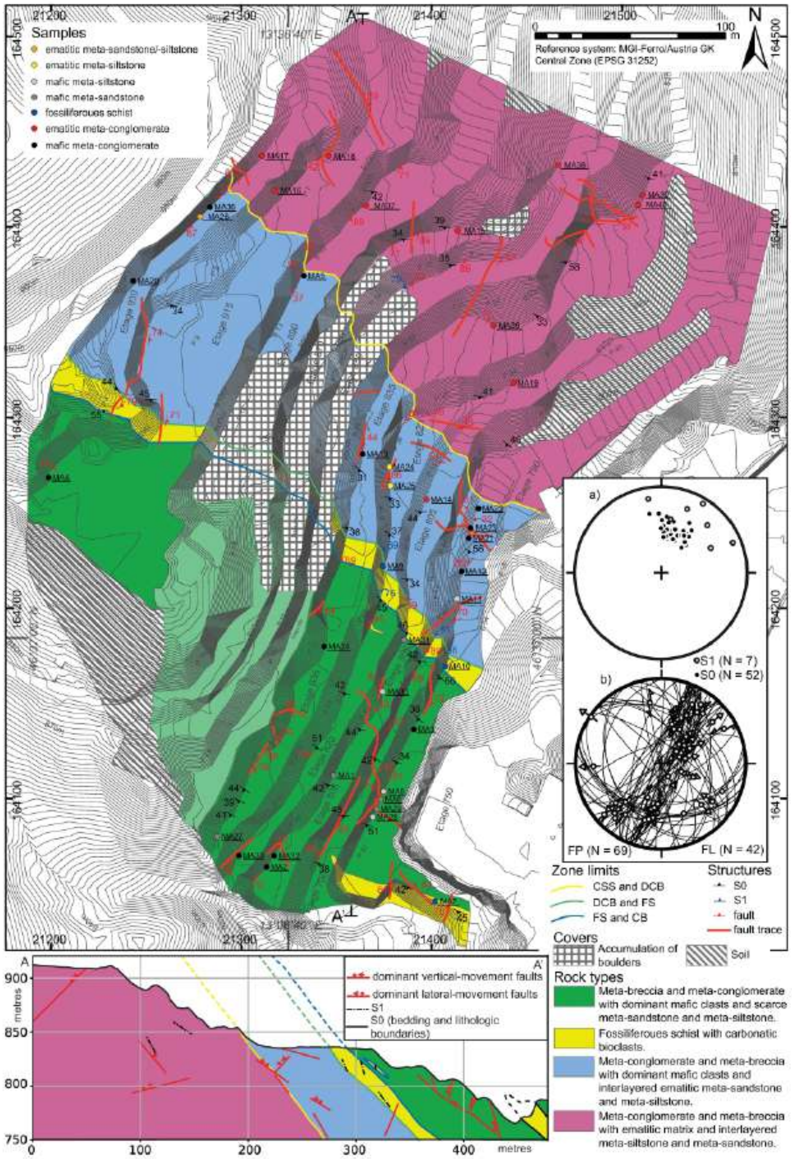

Figure 2. Geological map of the Jakomini quarry mapped in mid-December 2017 and N-S geological cross-section. Worsche Vermessung provided the base map. Pale colours indicate the inaccessible parts of the quarry during the fieldwork. In the inset equal area stereographic projection, lower hemisphere, with number of orientation data (N): a) pole to plane of bedding (S0) and S1 foliation; b) planes of fault surface (FP) and linear kinematic indicators (FL).

214x302mm (600 x 600 DPI)

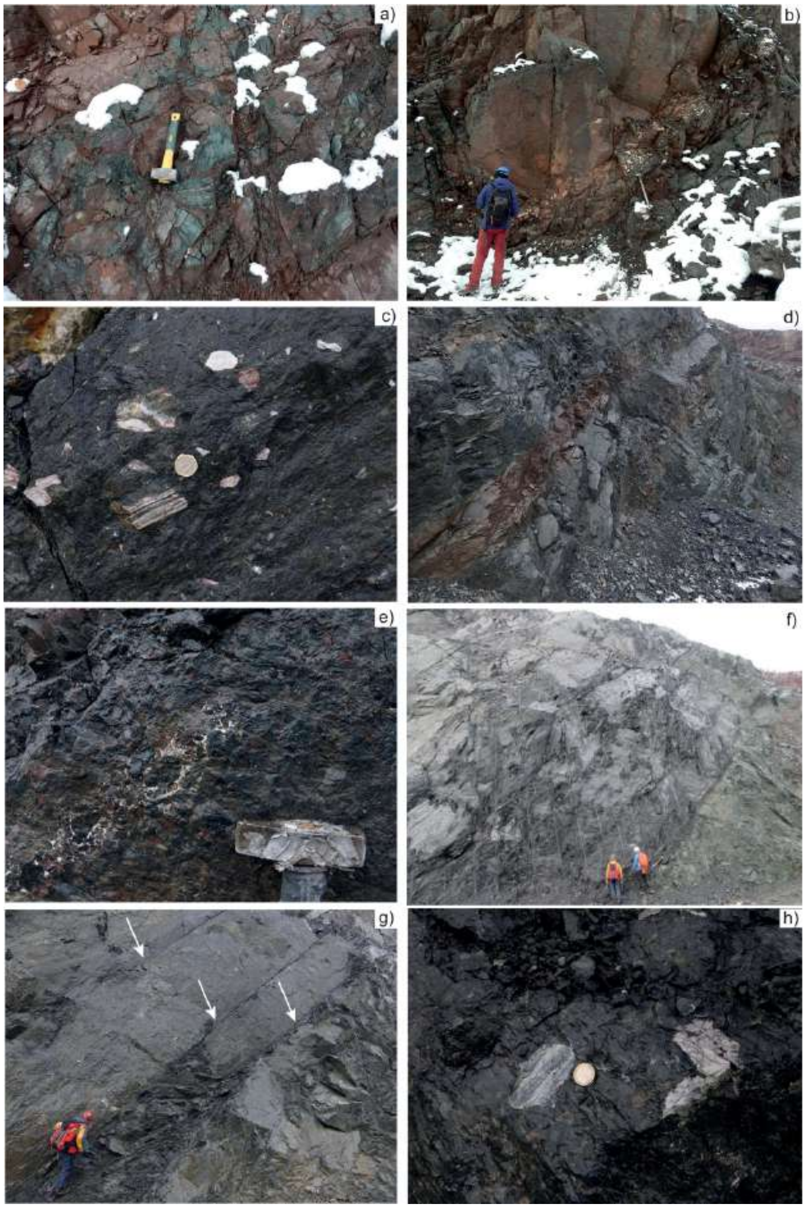

Figure 3. a) Metabasic clasts embodied in the red matrix intersected by fracture systems in CSS. b) Decimetre-thick conglomeratic breccia bed with angular marble clasts and minor metabasic clasts, in CSS. c) Angular to subrounded metabasic and marble clasts in the mafic conglomerate of DCB. d) Decimetre-thick red sandstone and siltstone beds within the mafic conglomerate of DCB. e) Centimetre-thick layer of conglomerate in DCB that is cemented by calcite. f) Boundary between brachiopod rich shale strata of sector FS and the greenish sandstone of DCB. g) Centimetre-thick mafic siltstone and pelite beds (white arrows) marking the boundary of conglomerate beds in CB. h) Rounded metabasic and marble clasts in the conglomerate of CB.

192x289mm (600 x 600 DPI)

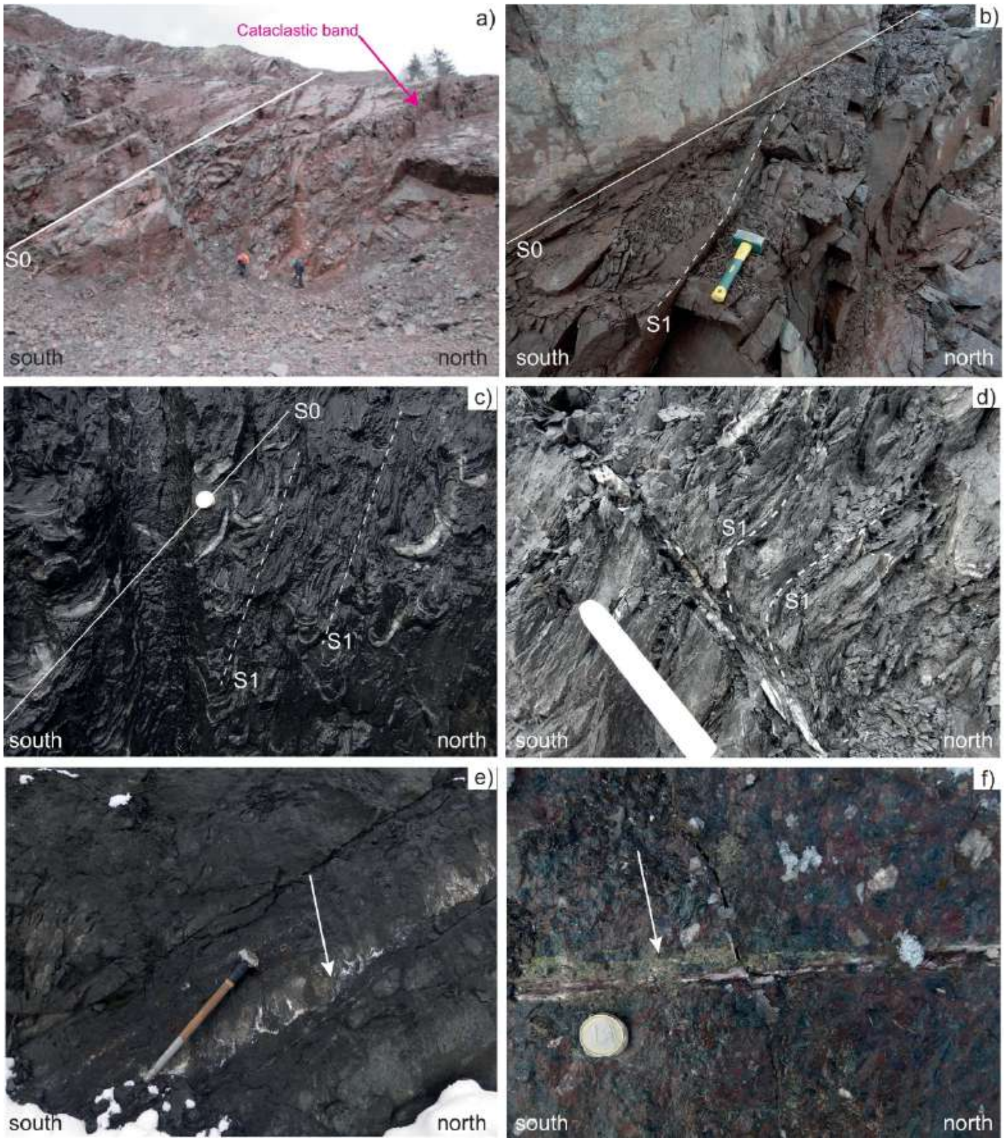

Figure 4. a) Bedded red conglomerate, sandstone, and siltstone of CSS that are intersected by cataclastic bands and fracture systems. b) Decimetre-thick beds of siltstone and sandstone of CSS with S1 foliation recorded only in siltstone; c) Brachiopod rich shale that records the S1 foliation intersecting the bedding (S0) in FS; coin for scale. d) Calcite veins in a cm-thick shear zone deflecting S1 foliation in fossiliferous carbonatic schist of FS; ink marker for scale. e) Fault surface with calcite fibres in the schist of FS. f) Centimetre-thick vein filled by epidote and chlorite in the conglomeratic breccia of CB.

192x217mm (600 x 600 DPI)

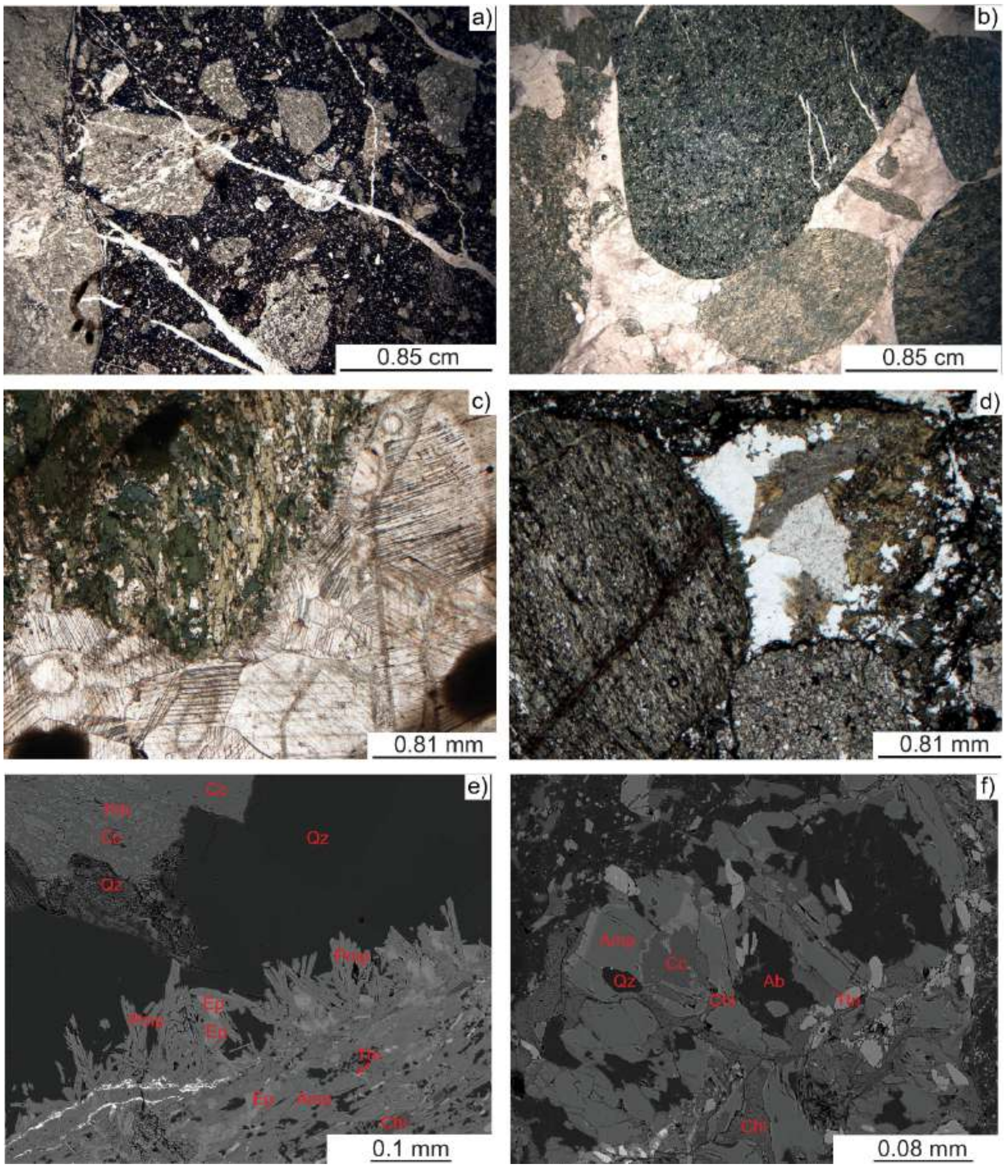

Figure 5. a) Sample MA17, CSS, meta-conglomerate with sub-rounded to angular clasts surrounded by hematite matrix and intersected by calcite veins; plane polarised light; b) Sample MA12, DCB, meta-conglomerate with dominant rounded metabasic clasts in recrystallised calcite cement; plane polarised light; c) Sample MA12, DCB, detail on twinning in polygonal calcite around a foliated metabasic clast; plane polarised light; d) Sample MA20, DCB, interstitial coarse-grained quartz and calcite crystals with pumpellyite radial to the clast surface; plane polarised light; e) Sample MA20, DCB, close up of previous photo with pumpellyite (Pmp) crystals radial to the clast surface and associated with epidote (Ep) in contact with euhedral coarse-grained quartz (Qz) crystal; prehnite (Prh) is enclosed in calcite (Cc); backscattered electron image; f) Sample MA23, sector DCB, portion of brecciated amphibolite clast with amphibole (Amp) from the clast with a rim of coronitic blue amphibole (light grey) in contact with calcite (Cc); also chlorite (Chl) partly replace amphibole; backscattered electron image. Sample location is shown in Figure 2.

182x212mm (600 x 600 DPI)

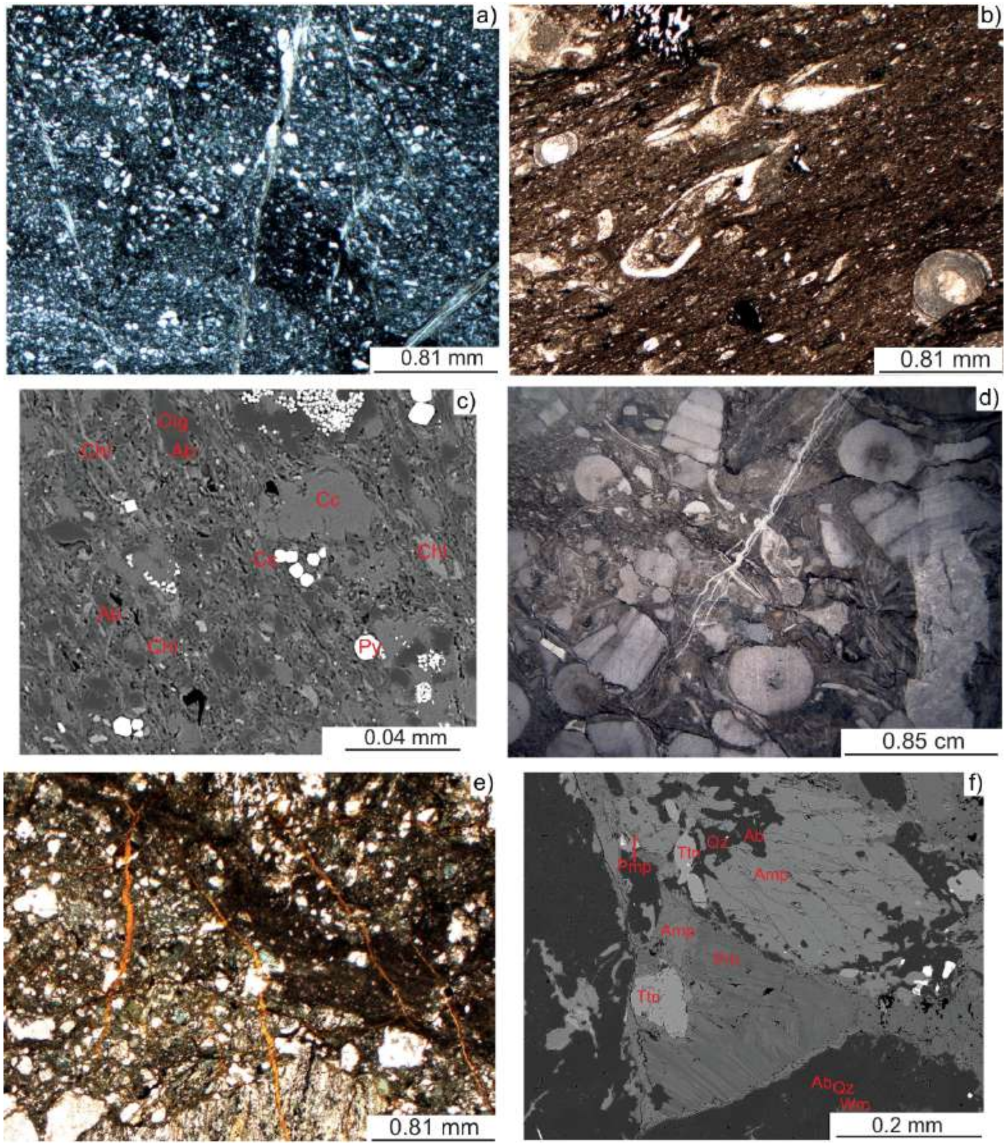

Figure 6. a) Sample MA25, DCB, meta-sandstone, sedimentary lamination intersected by quartz and chlorite veins; crossed polars; b) Sample MA10, FS, fossiliferous schist with stylolitic S1 foliation with brachiopod spines (L. Angiolini pers.com.) partly dissolved; plane polarised light; c) S1 marked by shape preferred orientation of chlorite (Chl), albite (Ab), and calcite (Cc); euhedral pyrite (Py) is scattered along the foliation; backscattered electron image; d) Sample MA7, FS, fossiliferous schist rich in crinoids that are partly dissolved along stylolitic S1 foliation that is intersected by sub-orthogonal calcite veins that collect the dissolved carbonate; plane polarised light; e) Sample MA33, meta-conglomerate of DC overprinted by a fault breccia, which is the finer-grained material (darker), intersected by chlorite veins; plane polarised light; f) Sample MA2, conglomerate of DC, prehnite (Prh) at the triple junction of leucoratic metagranitoid and amphibolite clasts; between prehnite a detrital titanite (Ttn) crystals is included; pumpellyite (Pmp) formed at the rim of amphibole (Amp) included in clasts; backscattered electron image. Sample location is shown in Figure 2.

182x207mm (600 x 600 DPI)

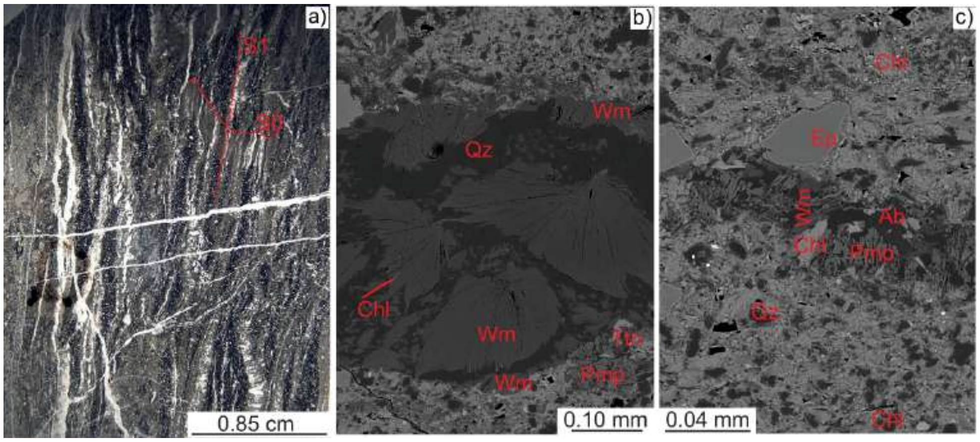

Figure 7. a) Sample MA28 meta-siltstone of CB in which the original stratigraphy (S0) is poorly preserved and S1 is the dominant fabric; S1 is intersected by subsequent generation of veins; plane polarised light; b) Sample MA28 meta-siltstone of CB; vein filled by white mica (Wm), quartz (Qz), and minor chlorite (Chl); close to the vein pumpellyite (Pmp) formed in the rock matrix; backscattered electron image; c) Sample MA28 meta-siltstone of CB; microscopic vein filled by pumpellyite (Pmp), albite (Ab), white mica (Wm), and chlorite (Chl); backscattered electron image. Sample location is shown in Figure 2.

195x84mm (600 x 600 DPI)

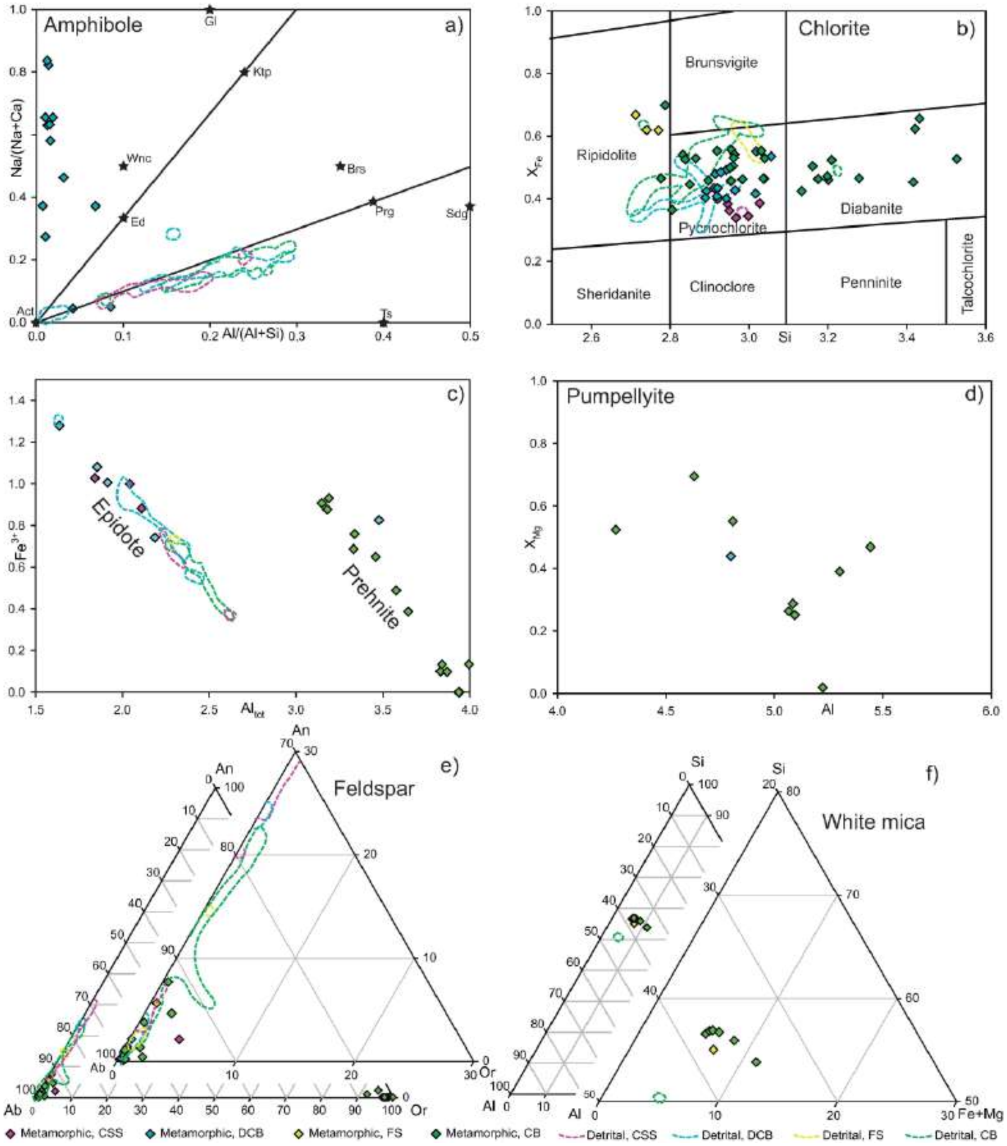

Figure 8. Composition of metamorphic minerals that overprint the sequences in the four zones. Fields delimitate the composition of detrital minerals (in clasts and detrital grains). a) Classification diagram for amphibole (Laird and Albee, 1981) with formula calculated on 23 oxygen atoms, according to Locock (2014); Gl = glaucophane; Ktp = katophorite; Brs = barroisite; Prg = pargasite; Sdg = sadaganaite; Ts = tschermakite; Act = actinolite; Ed = edenite; Wnc = winchite; b) Classification diagram for chlorite (Hey 1954) with formula calculated on 14 oxygen atoms, according to Bourdelle et al. (2013); c) Composition of epidote and prehnite with Fe3+ estimated on charge balance and formula based on 12.5 oxygen atoms and 14 cations, respectively; d) Composition of pumpellyite with formula based on 16 cations according to Cortesogno et al. (1984); e) Composition of feldspar with formula based on 8 oxygen atoms; f) Composition of white mica with formula based on 11 oxygen atoms.

201x229mm (600 x 600 DPI)

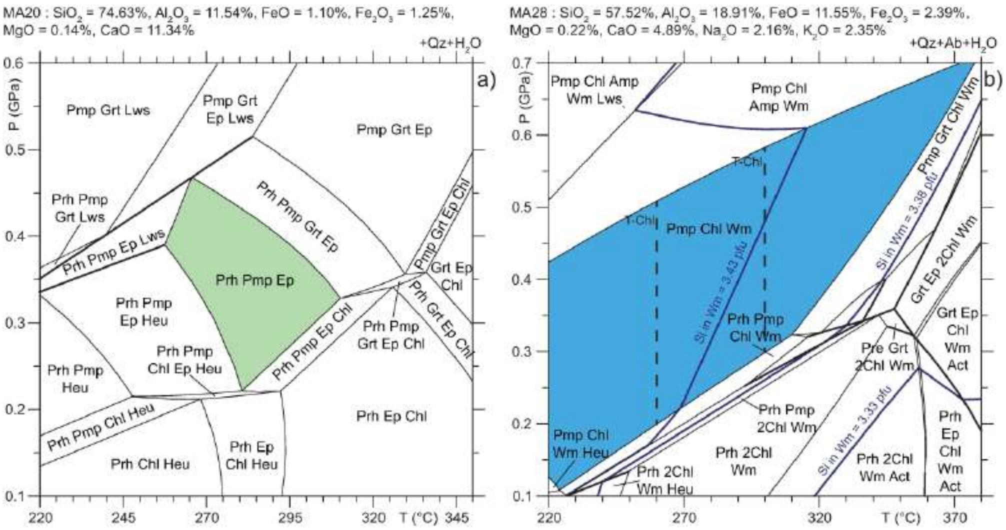

Figure 9. a) CFMASHO phase diagram that models the stability field of mineralised interstices between metabasite clasts in MA20 meta-conglomerate. The bulk composition determined on the modal amount of metamorphic minerals is reported at the top of the diagram. The Pre + Pmp + Ep + Qz + H2O stability field is coloured in green. Univariant lines are double thickness. b) KNCFMASHO phase diagram that models the stability field of mineralised veins in MA28 meta-siltite. The bulk composition determined on the modal amount of metamorphic minerals is reported at the top of the diagram. The Pmp + Chl + Wm + Ab + Qz + H2O stability field is coloured in light blue. Si-in white mica isopleths (apfu) are tracked in dark blue. Small fields were not labelled. Univariant lines are double thickness.

194x101mm (600 x 600 DPI)

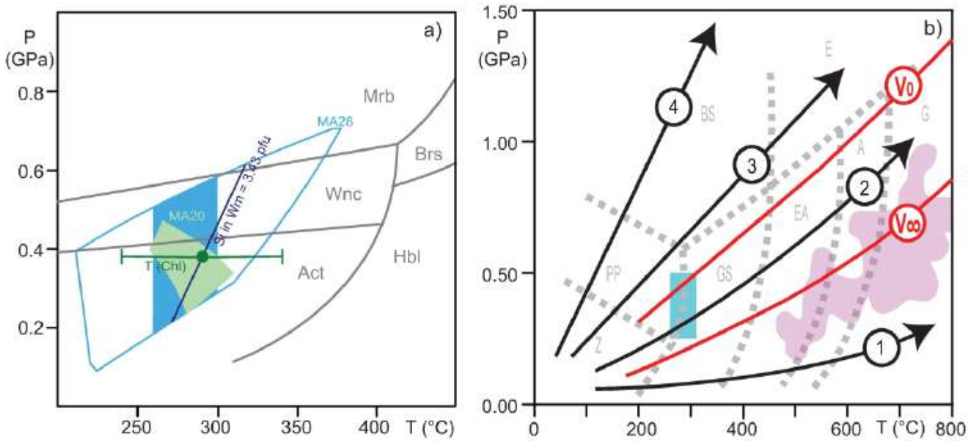

Figure 10. a) Summary of PT conditions determined for the Badstub Formation metasedimentary rocks with different thermobarometric methods. Stability fields of actinolite (Act), winchite (Wnc), magnesioriebeckite (Mrb), barroisite (Brs), and hornblende (Hbl) are from Banno et al. (1984). The results converge to T = 260 - 310 °C and P = 0.25 - 0.50 GPa. b) Metamorphic conditions determined for the Badstub Formation (cyan rectangle) compared with the petrogenetic PT grid (modified after Ernst 1976) with black-thick lines representing geothermal gradients traditionally associated to arc regions (1), plate interior (2), warm subduction zones (3) and cold subduction zones (4), according to Cloos (1993), and red-thick lines representing stable (V0) and relaxed (V∞) geotherms, according to England and Thompson (1984). Labels of metamorphic facies: Z: zeolite; PP: prehnite-pumpellyite; BS: blueschist; GS: greenschist; EA: epidote amphibolite; A: amphibolite; E: eclogite; G: granulite. The pink area represents the PT field of Permian-Triassic metamorphic imprints recorded in the continental crustal units of the Alps (Roda et al. 2019 and references therein).

205x90mm (600 x 600 DPI)

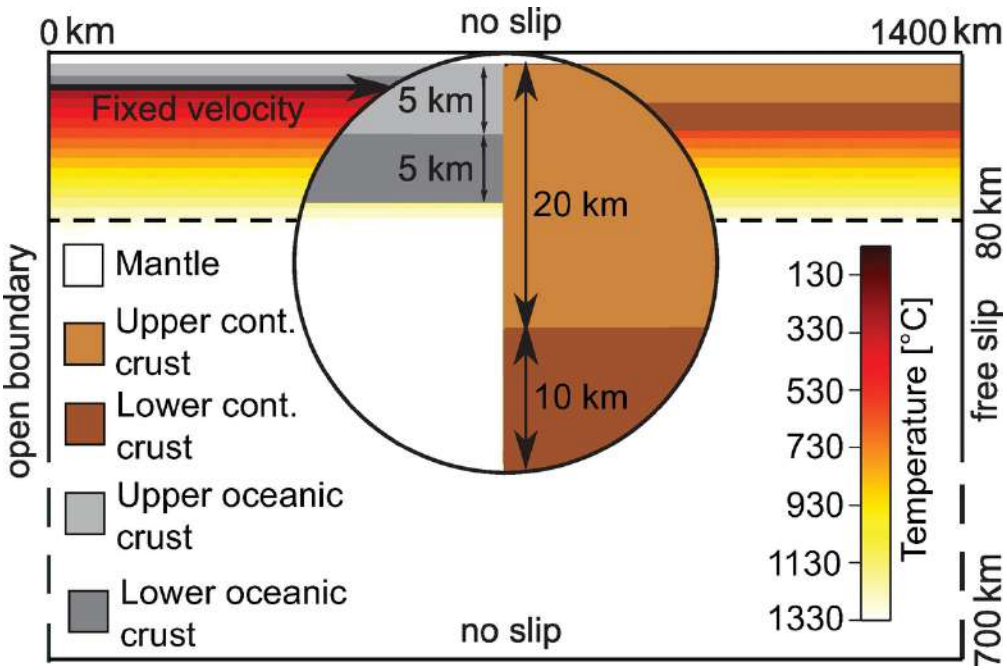

Figure 11. Model setup. The model domain is 1400 km wide and 700 km deep. The Earth's surface has been treated by means of a 10 km-thick sticky-air. The characteristic compositions of lower and upper continental crust, oceanic crust, and lithospheric mantle of the upper plate have been differentiated by means of markers distributed regularly with a density of 1 marker per 0.25 km^2. The velocity boundary conditions correspond to no-slip conditions along the upper and the lower boundaries of the 2D domain and free-slip conditions along the right boundary. In addition, a velocity of 3 cm yr^{-1} has been prescribed at the bottom of the oceanic crust and along a 45° dipping plane that extends from the trench to a depth of 100 km, to facilitate the trigger of the subduction. The thermal boundary conditions correspond to fixed temperatures at the top (27 °C = 300 K) and at the bottom (1327 °C = 1600 K) of the model and zero thermal flux at the vertical sidewalls. The initial thermal structure is characterised by a simple conductive thermal configuration throughout the lithosphere, with temperatures that increase linearly from the surface to its base located at a depth of 80 km, and a constant temperature of 1327 °C below the lithosphere.

100x66mm (300 x 300 DPI)

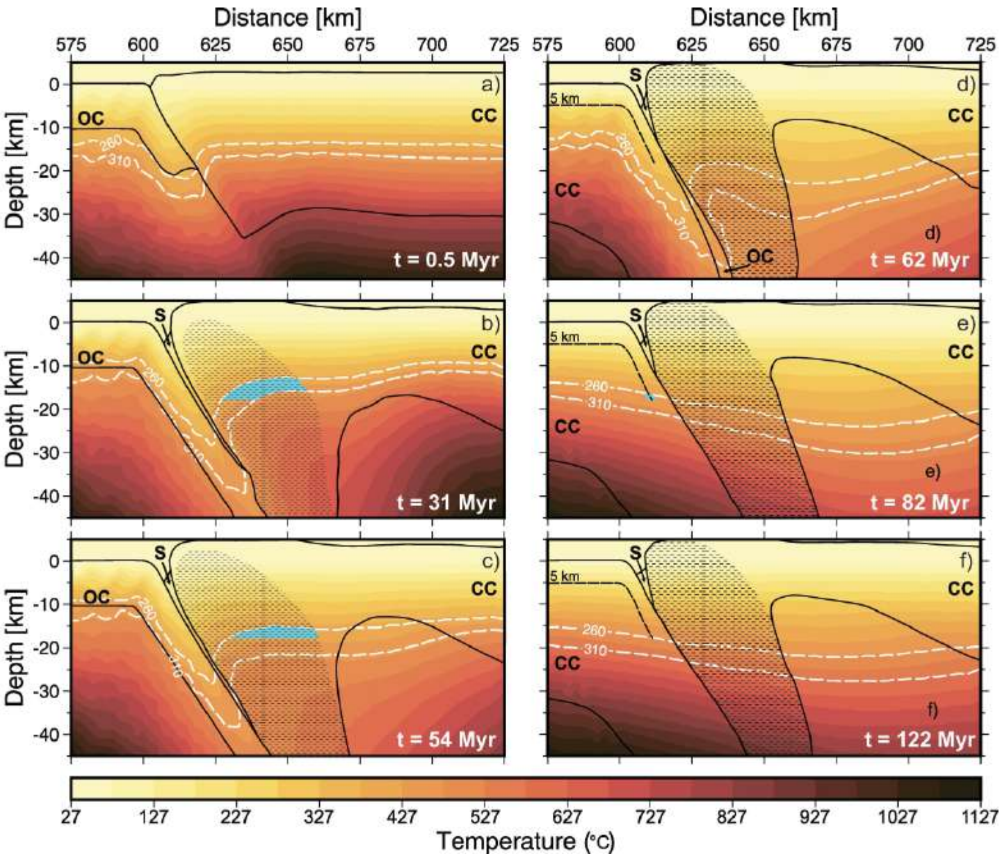

Figure 12. Thermal field of the model for 122 Myr of convergence, from subduction (a, b, c) to continental collision and gravitational requilibration (d, e, f). Black solid lines represent crustal boundaries (OC = oceanic crust; CC = continental crust; S = trench sediments). Isotherms 260 and 310 °C are reported as white dashed lines. The orogenic wedge is enclosed in the shaded area. The PT conditions inferred for the metamorphism of Badstub Formation (T = 260 - 310 °C and P = 0.25 - 0.5 GPa) in the continental crust are indicated by cyan area. In the upper plate these conditions are confined within the orogenic wedge where tectonic burial occurs, whereas in the lower plate these conditions are constrained by 5 km of sedimentary sequences above the Badstub Formation indicated with the black dashed line. Model results indicate that the metamorphic conditions recorded by the Badstub Formation are potentially achieved in the upper plate during oceanic subduction or in the lower plate during continental subduction at a depth of 13 - 18 km and 16 - 18 km, respectively. Colour map after Crameri (2018).

198x167mm (600 x 600 DPI)

Formation	**rocks**	**sedimetary environment**	**age**
Nötsch	siltstone and shale with polymictic conglomerate and limestone	turbidites	Early Kasimovian - Late Visean
Badstub	amphibolite breccia, conglomerate, sandstone, and siltstone	submarine deposits in a proximal fan or slope environment	
Erlachgraben	polymictic conglomerate, immature sandstone, siltstone, and shale	submarine debris flows, turbidity currents, hemipelagic deposits	

Supp. Table 1. Summary of rock types, sedimentary environments, and ages of the Carboniferous of Nötsch (Krainer and Mogessie 1991; Krainer 1992; Schönlaub and Heinisch 1994; Krainer and Vachard 2002; Hubmann *et al.* 2006; Ebner *et al.* 2008; Vachard *et al.* 2018).

	Si	Al^{VI}	Al^{VI}	Fe^{3+}	Fe^{2+}	Mg	Ca	Na	T(°C)
Amphibole									
Ferro-ferri-winchite (DCB)	NS	0.02 - 0.38	0.02 - 0.17	0.83±0.42	2.30±0.26	1.70±0.34	0.99±0.31	0.97±0.34	NC
Ribekite (DCB)	NS	0.04±0.01	0.07±0.02	1.50±0.10	1.97±0.18	1.37±0.06	0.36	1.64	NC
Actinolite (DCB)	NS	0.04 - 0.41	0.05 - 0.30	0.01 - 0.35	1.90±0.35	2.72±0.45	1.79±0.24	0.02 - 0.47	NC
Chlorite									
matrix (CSS, DCB, CB)	2.94±0.09	1.05±0.09	1.17±0.08	NC	2.17±0.34	2.47±0.28	NS	NS	293±52
coronitic (CSS, DCB, CB)	3.00±0.06	1.00±0.06	1.17±0.08	NC	2.13±0.43	2.52±0.37	NS	NS	262±65
veins (DCB, FS, CB)	3.09±0.31	0.91±0.31	1.24±0.14	NC	2.46±0.32	2.05±0.43	NS	NS	279±53
micro-shear zones (CSS, CB)	3.18±0.17	0.82±0.17	1.06±0.07	NC	2.13±0.17	2.61±0.14	NS	NS	207±69
Epidote									
With Pmp (DCB)	NS	0.02±0.01	1.87±0.23	1.03±0.22	NS	NS	NS	NS	NC
matrix and SZ (CSS)	NS	0.00-0.06	1.98±0.13	0.97±0.08	NS	NS	NS	NS	NC
Pumpellyite									
veins (CB)	6.02±0.03	0.01±0.01	5.08±0.01	0	0.75±0.02	0.27±0.02	NS	NS	NC
matrix (CB)	6.10±0.08	0	4.57±0.28	0.27±0.23	0.49±0.14	0.69±0.06	NS	NS	NC
coronitic (DCB, CB)	6.02±0.03	0-0.02	5.16±0.25	0-0.19	0.57±0.20	0.26±0.15	NS	NS	NC
Prehnite									
lamellae (CB)	5.98±0.03	0.03±0.02	3.5±0.33	0.44±0.36	0-0.14	0.01±0.01	NS	NS	NC
DBC	5.85	0.15	3.33	0.83	0	0	NS	NS	NC
White mica									
veins (CB)	3.42±0.04	0.58±0.04	1.64±0.08	NC	0.19±0.11	0.25±0.03	0	0	NC
matrix (FS)	3.34	0.66	1.65	NC	0.20	0.23	0.04	0.05	NC

Supp. Table 2. Summary of mineral composition shown by means of average and standard deviation or maximum and minimum values of cations from the stoichiometric formulae. In brackets the quarry sector is indicated. NC = not calculated, NS = not shown.

	rim of detrital grain	rim of detrital grain	rim of detrital grain
Sample	MA23-2-114	MA23-2-115	MA23-C2-01
Analysis (wt%)			
SiO_2	53.04	53.55	53.72
TiO_2	0.10	0.00	0.05
Al_2O_3	0.56	0.63	2.00
Cr_2O_3	0.00	0.04	0.02
MnO	1.16	0.64	0.55
FeO	26.64	27.42	17.15
NiO	0.00	0.00	0.02
MgO	6.29	6.39	12.98
CaO	4.73	2.24	12.07
Na_2O	4.44	5.72	0.31
K_2O	0.02	0.01	0.04
Cl	0.02	0.00	
Initial Total	97.01	96.65	98.91
OUTPUT			
$Fe^{3+}/\Sigma Fe$ used	0.33	0.46	0.05
Final wt% values			
MnO	1.16	0.64	0.55
FeO	17.93	14.81	16.31
Fe_2O_3	9.68	14.02	0.93
H_2O+	1.99	2.01	2.05
Total	99.97	100.06	101.05
Group	OH,F,Cl	OH,F,Cl	OH,F,Cl
Subgroup of (OH,F,Cl)	Na-Ca	Na	Ca
Species	ferro-ferri-winchite	riebeckite	actinolite
T (ideally 8 apfu)			
Si	7.98	7.97	7.78
Al	0.02	0.03	0.22
T subtotal	8.00	8.00	8.00
C (ideally 5 apfu)			
Ti	0.01		0.01
Al	0.08	0.08	0.12
Cr		0.01	0.00
Fe^{3+}	1.10	1.57	0.10
Ni			0.00
Mn^{2+}	0.15	0.08	
Fe^{2+}	2.26	1.84	1.97
Mg	1.41	1.42	2.80
C subtotal	5.00	5.00	5.00
B (ideally 2 apfu)			
Mn^{2+}			0.07
Fe^{2+}			0.01

Ca	0.76	0.36	1.87
Na	1.24	1.64	0.05
B subtotal	2.00	2.00	2.00
A (from 0 to 1 apfu)			
Na	0.06	0.01	0.03
K	0.00	0.00	0.01
A subtotal	0.06	0.01	0.04
O (non-W)	22.00	22.00	22.00
W (ideally 2 apfu)			
OH	1.99	2.00	2.00
Cl	0.01	0.00	
W subtotal	2.00	2.00	2.00
Sum T,C,B,A	15.06	15.01	15.04

	with Prh	with Wnc & Cc	in vein with Pmp	matrix	matrix
Sample	MA2-1-61	MA23-2-118	MA28-1-48	MA29-1-28	MA33-1-23
Analysis (wt%)					
SiO2	27.49	28.50	25.72	28.04	28.70
TiO2	0.00	0.05	0.00	0.03	0.06
Al2O3	17.55	17.75	20.45	17.62	14.19
FeO	29.18	23.11	34.34	28.36	26.17
MnO	0.28	0.55	0.38	0.35	0.23
MgO	13.02	17.39	8.29	14.04	14.45
CaO	0.16	0.35	0.12	0.26	0.79
Na2O	0.00	0.01	0.00	0.02	0.03
K2O	0.01	0.02	0.04	0.03	0.05
Cr2O3	0.03	0.00	0.01	0.01	0.00
NiO	0.00	0.02	0.03	0.01	0.00
Cl	0.01	0.00	0.02	0.01	0.01
Sum	87.72	87.75	89.40	88.80	84.69
formula: 14 O					
Si	2.95	2.96	2.79	2.96	3.16
Ti	0.00	0.00	0.00	0.00	0.00
Al	2.22	2.18	2.61	2.19	1.84
Fe2+	2.62	2.01	3.11	2.50	2.41
Mn	0.03	0.05	0.03	0.03	0.02
Mg	2.09	2.70	1.34	2.21	2.37
Ca	0.02	0.04	0.01	0.03	0.09
Na	0.00	0.00	0.00	0.00	0.01
K	0.00	0.00	0.00	0.00	0.01
Cr	0.00	0.00	0.00	0.00	0.00
Ni	0.00	0.00	0.00	0.00	0.00
Cl	0.00	0.00	0.00	0.00	0.00

vein	with Cc	in shear zone	rim of Amp	in shear zone	in vein
MA10-1-2	MA12-1-23	MA4-1-123	MA17-1-57	MA17-2-78	MA26-1-135
25.77	27.84	31.38	30.14	28.83	28.16
0.05	0.05	0.00	0.04	0.06	0.03
21.59	17.44	14.18	19.67	18.45	17.98
30.73	26.53	25.22	18.43	21.08	26.67
0.22	0.41	0.29	0.59	0.66	0.57
10.58	14.59	16.23	19.68	19.03	15.44
0.19	0.68	0.51	0.29	0.04	0.05
0.01	0.03	0.03	0.02	0.01	0.00
0.00	0.04	0.02	0.02	0.03	0.00
0.01	0.00	0.00	0.01	0.00	0.00
0.00	0.06	0.04	0.00	0.03	0.00
0.01	0.00	0.02	0.00	0.00	0.00
89.15	87.67	87.93	88.91	88.21	88.90
2.74	2.96	3.28	3.00	2.95	2.94
0.00	0.00	0.00	0.00	0.00	0.00
2.71	2.18	1.75	2.31	2.22	2.21
2.73	2.36	2.20	1.53	1.80	2.33
0.02	0.04	0.03	0.05	0.06	0.05
1.68	2.31	2.53	2.92	2.90	2.40
0.02	0.08	0.06	0.03	0.00	0.01
0.00	0.01	0.01	0.00	0.00	0.00
0.00	0.01	0.00	0.00	0.00	0.00
0.00	0.00	0.00	0.00	0.00	0.00
0.00	0.01	0.00	0.00	0.00	0.00
0.00	0.00	0.00	0.00	0.00	0.00

	matrix	shear zone	matrix	matrix
Sample	MA20-1-147	MA20-1-148	MA17-1-61	MA17-2-77
Analysis (wt%)				
K2O	0.00	0.00	0.01	0.00
CaO	22.96	23.21	21.09	23.38
TiO2	0.00	0.07	0.35	0.04
Cr2O3	0.01	0.00	0.00	0.00
MnO	0.16	0.57	0.41	0.13
FeO	15.24	10.75	15.74	13.25
NiO	0.00	0.01	0.05	0.03
Na2O	0.01	0.00	0.00	0.01
SiO2	35.00	36.02	36.19	37.63
Al2O3	18.56	22.49	21.35	22.48
MgO	0.00	0.03	0.53	0.03
TOTAL	91.94	93.15	95.72	96.98
formula: 8 cations and 12.5 O, Fe3+=3-Alvi-Ti-Cr				
Si	2.97	2.97	2.94	3.00
Al.IV	0.03	0.03	0.06	0.00
Al.VI	1.82	2.16	1.98	2.11
Ti	0.00	0.00	0.02	0.00
Cr	0.00	0.00	0.00	0.00
Fe3+	1.08	0.74	1.00	0.88
Fe2+	0.00	0.00	0.07	0.00
Mg	0.00	0.00	0.06	0.00
Ni	0.00	0.00	0.00	0.00
Mn	0.01	0.04	0.03	0.01
Ca	2.09	2.05	1.83	1.99
Na	0.00	0.00	0.00	0.00
K	0.00	0.00	0.00	0.00
FeO	0.00	0.00	1.02	0.00
Fe2O3	16.94	11.95	16.35	14.72
Total.calc	93.64	94.35	97.36	98.45

	rim on Amp	vein	intraclast	intraclast
Sample	MA12-1-28	MA28-1-55	MA2-3-118	MA2-3-118
Analysis (wt%)				
SiO2	37.10	37.65	37.58	37.58
TiO2	0.19	0.06	0.15	0.15
Al2O3	25.27	24.62	22.18	22.18
Cr2O3	0.03	0.02	0.00	0.00
FeO tot	5.63	5.10	7.83	7.83
MnO	0.05	0.09	0.09	0.09
MgO	1.84	3.17	2.77	2.77
CaO	23.07	22.75	21.62	21.62
Na2O	0.00	0.04	0.07	0.07
K2O	0.00	0.01	0.07	0.07
NiO	0.04	0.00	0.00	0.00
Sum	93.22	93.51	92.36	92.36
formula on 16 cations				
Si	5.98	6.01	6.14	6.14
Ti	0.02	0.01	0.02	0.02
Al	4.80	4.63	4.27	4.27
Cr	0.00	0.00	0.00	0.00
Fe 3+	0.19	0.35	0.46	0.46
Fe 2+	0.56	0.33	0.61	0.61
Mn	0.01	0.01	0.01	0.01
Mg	0.44	0.75	0.67	0.67
Ca	3.98	3.89	3.78	3.78
Na	0.00	0.01	0.02	0.02
K	0.00	0.00	0.01	0.01
Ni	0.01	0.00	0.00	0.00

Sample	intraclast MA2-1-59	intraclast MA2-1-62	intraclast MA2-1-67	intraclast MA2-1-68	intraclast MA2-2-88	intraclast MA2-3-111
Analysis (wt%)						
SiO2	41.86	42.75	41.87	42.05	43.39	42.96
TiO2	0.05	0.06	0.00	0.01	0.09	0.02
Al2O3	20.68	24.42	19.74	19.99	23.40	23.29
Cr2O3	0.00	0.00	0.01	0.00	0.01	0.02
FeO tot	5.81	1.24	6.24	6.49	1.50	1.34
MnO	0.00	0.10	0.04	0.01	0.11	0.13
MgO	0.00	0.07	0.03	0.05	0.02	0.00
CaO	25.69	26.02	25.45	25.77	26.35	26.51
Na2O	0.00	0.06	0.03	0.04	0.03	0.00
K2O	0.00	0.00	0.01	0.01	0.00	0.00
NiO	0.00	0.03	0.00	0.00	0.07	0.00
Sum	94.09	94.75	93.42	94.42	94.97	94.27
formula based on 14 cations						
Si	5.94	5.94	6.00	5.96	6.03	6.01
Ti	0.01	0.01	0.00	0.00	0.01	0.00
Al	3.46	4.00	3.33	3.34	3.83	3.84
-Al IV	0.06	0.06	0.00	0.04	0.00	0.00
-AL VI	3.40	3.93	3.33	3.29	3.83	3.84
Fe 3+	0.65	0.13	0.69	0.76	0.10	0.13
Fe 2+	0.04	0.01	0.06	0.01	0.07	0.02
Cr	0.00	0.00	0.00	0.00	0.00	0.00
Mn	0.00	0.01	0.00	0.00	0.01	0.02
Mg	0.00	0.01	0.01	0.01	0.00	0.00
Ca	3.91	3.87	3.90	3.91	3.92	3.97
Na	0.00	0.02	0.01	0.01	0.01	0.00
K	0.00	0.00	0.00	0.00	0.00	0.00
Ni	0.00	0.00	0.00	0.00	0.01	0.00

	vein	vein	matrix	on S1	vein	vein
Sample	MA17-1-53	MA17-1-54	MA23-2-112	MA10-1-7	MA28-1-33	MA28-1-36
Analysis (wt%)						
K2O	0.03	15.68	0.04	0.09	0.05	15.43
CaO	0.06	0.02	0.12	1.20	0.12	0.08
TiO2	0.02	0.03	0.02	0.03	0.00	0.00
Cr2O3	0.00	0.00	0.03	0.03	0.00	0.00
MnO	0.00	0.00	0.00	0.00	0.00	0.03
FeO	0.02	0.22	0.31	0.25	0.10	0.06
NiO	0.00	0.00	0.00	0.01	0.00	0.05
Na2O	10.88	0.16	11.34	11.00	11.59	0.10
SiO2	69.63	66.51	69.56	67.87	68.34	66.01
Al2O3	20.01	18.76	19.89	20.93	19.89	18.49
MgO	0.01	0.00	0.10	0.00	0.01	0.00
TOTAL	100.66	101.38	101.41	101.41	100.10	100.25
formula based on 8 O						
Si	3.01	3.01	2.99	2.93	2.98	3.02
Al	1.02	1.00	1.01	1.07	1.02	1.00
Ti	0.00	0.00	0.00	0.00	0.00	0.00
Cr	0.00	0.00	0.00	0.00	0.00	0.00
Fe2+	0.00	0.01	0.01	0.01	0.00	0.00
Mn	0.00	0.00	0.00	0.00	0.00	0.00
Mg	0.00	0.00	0.01	0.00	0.00	0.00
Ni	0.00	0.00	0.00	0.00	0.00	0.00
Ca	0.00	0.00	0.01	0.06	0.01	0.00
Na	0.91	0.01	0.95	0.92	0.98	0.01
K	0.00	0.91	0.00	0.00	0.00	0.90
XAn	0.30	6.46	0.58	5.69	0.57	30.66
Xsan	0.18	98.37	0.23	0.51	0.28	98.60
Xab	99.52	1.53	99.19	93.84	99.15	0.97

intraclast	shear zone	shear zone	matix
MA2-1-65	MA4-1-128	MA4-1-129	MA29-1-34
0.07	15.66	0.08	14.05
0.80	0.04	1.58	0.03
0.05	0.03	0.00	0.04
0.00	0.00	0.00	0.00
0.02	0.00	0.02	0.00
0.35	0.38	0.27	0.43
0.01	0.00	0.00	0.03
11.16	0.27	10.40	0.30
65.68	64.15	65.05	63.79
20.50	18.87	21.15	19.47
0.00	0.03	0.05	0.01
98.64	99.43	98.60	98.15
2.92	2.98	2.90	2.97
1.08	1.03	1.11	1.07
0.00	0.00	0.00	0.00
0.00	0.00	0.00	0.00
0.01	0.01	0.01	0.02
0.00	0.00	0.00	0.00
0.00	0.00	0.00	0.00
0.00	0.00	0.00	0.00
0.04	0.00	0.08	0.00
0.96	0.02	0.90	0.03
0.00	0.93	0.00	0.83
3.81	7.57	7.75	5.24
0.40	97.24	0.46	96.69
95.81	2.55	91.83	3.14

	metamorphic in matrix	radial in veins	in veins with Pmp
Sample	MA10-2-13	MA28-1-41	MA28-1-47
Analysis (wt%)			
K2O	7.75	9.23	8.32
CaO	0.59	0.03	0.05
TiO2	0.22	0.00	0.00
Cr2O3	0.03	0.00	0.00
MnO	0.00	0.05	0.02
FeO	3.59	2.88	4.90
NiO	0.08	0.02	0.01
Na2O	0.35	0.01	0.01
SiO2	49.49	53.28	51.71
Al2O3	28.89	29.13	27.99
MgO	2.26	2.60	2.45
TOTAL	93.25	97.23	95.46
Formula based on 11 O			
Si (T)	3.34	3.44	3.43
Al total	2.30	2.22	2.19
Al.iv (T)	0.66	0.56	0.57
Al.vi (M2)	1.65	1.66	1.61
Ti (M2)	0.01	0.00	0.00
Cr (M2)	0.00	0.00	0.00
Mn (M2)	0.00	0.00	0.00
Ni (M2)	0.00	0.00	0.00
Fe2+total	0.20	0.16	0.27
Fe2+ (M2)	0.20	0.16	0.27
Mg.total	0.23	0.25	0.24
Mg (M2)	0.23	0.25	0.24
Fe 2+ (M1)	0.00	0.00	0.00
Mg (M1)	0.00	0.00	0.00
Ca (M1)	0.04	0.00	0.00
Vac. (M1)	0.91	0.93	0.87
Na (A)	0.05	0.00	0.00
K (A)	0.67	0.76	0.70

	Rheology	E (kJ mol^{-1})	n	μ_0 (Pa s)	ρ_0 (kg m^{-3})	K (W m^{-1} K-^{1})	Hc (μW m^{-3})	Refs
Continental crust	Dry granite	123	3.2	3.47E+21	2640	3.03	2.5	1,2,3,4
Upper oceanic crust	-	-	-	1.00E+19	2961	2.1	0.4	3,4,5,6,7,8
Lower oceani crust	Diabase	260	2.4	1.61E+22	2961	2.1	0.4	9,1,3,4,6
Mantle	Dry dunite	444	3.4	5.01E+20	3200	4.15	0.002	10,9,2,3,4,8
Serpentine	-	-	-	1.00E+19	3000	4.15	0.002	2,3,11,4,12,7

Supp. Table 4. Thermal and rheological parameters. References: (1) Ranalli and Murphy (1987); (2) Haenel et al. (1988); (3) Dubois and Diament (1997); (4) Best and Christiansen (2001); (5) Gerya and Yuen (2003); (6) Afonso and Ranalli (2004); (7) Gerya and Stoeckhert (2006); (8) Roda et al. (2012); (9) Kirby (1983); (10) Chopra and Peterson (1981); (11) Schmidt and Poli (1998); (12) Roda et al. (2011).